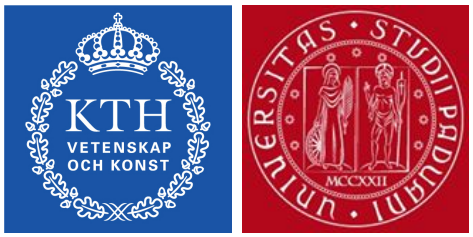

KUNGLIGA TEKNISKA HÖGSKOLAN
UNIVERSITÅ DEGLI STUDI DI PADOVA

DIPARTIMENTO DI INGEGNERIA INDUSTRIALE
CORSO DI LAUREA IN INGEGNERIA DEI MATERIALI

Slow Strain Rate Tensile Tests on Notched OFP-Copper Bars

Internal Supervisor: prof.ssa Irene Calliari
External Supervisor: prof. Rolf Sandström

Candidate: Silvia Di Giannantonio

Matr. 1036610

Academic year 2014-2015

å ä ö

Contents

Abstract

In Sweden, spent nuclear fuel is planned to be placed in waste packages with an external cylindrical OFP-copper canister according to the KBS-3 concept, developed by the SKB. The canisters will be exposed to an external pressure of about 15 MPa due to the hydrostatic pressure from a 500m water pillar and the swelling pressure from the surrounding bentonite clay. Due to this pressure the canisters will be subjected to creep under multiaxial stress state. For it is likely that the increase in pressure will be slow and gradual, the ideal tool to simulate this type of loading is slow strain rate tensile tests (SSRT).

In the present work circumferentially double nothced bars with a Bridgman notch geometry were tested uniaxially with $10^{-6}1/s$ and $10^{-7}1/s$ strain rate, at 75℃ and 125℃. Three were the chosen notch acuity , namely 5, 2 and 0.5 and two smooth specimens were tested to provide the uniaxial term of comparison. Both the yield strength and maximum strength were found to be higher for specimens with higher notch acuity. Not the temperature, nor the strain rate were found to have an appreciable effect on material's strength parameters. On the other hand, the material's lifetime was found to be notch acuity dependent: the sharper the notch, the shorter the lifetime is.
The material's ductility was evaluated: specimens with the sharper notches showed the lower ductility. Different deformations on the two notches was observed and together with the overall strain to rupture, also the radial and axial strain on the notches were evaluated: not an evident relation between the parameters was found. Just for the broken notch's radial strain a linear, increasing trend with the notch acuity was found.
Finally, some metallographic investigation were made: more elongated grains along the stress direction were visible in the broken notches than in the unbroken ones. The results are in good agreement with the expectations but more tests are needed to be performed with different strain rates and different notches acuity.

1

Project Background: the disposal of spent nuclear fuel

This chapter provides a brief overview of the present project framework, in order to better understand its aim and objectives.

1.1 Nuclear Power Plants in Sweden

Nuclear power plants generate about 30% of the electricity produced in the EU. As of August 2014 there is a total of 184 nuclear power plant units as showed in Figure 1.1 which account for approximately 15% of total energy consumption. Some reactors are being decommissioned, others are having their working lives extended, and several new units are planned or under construction.

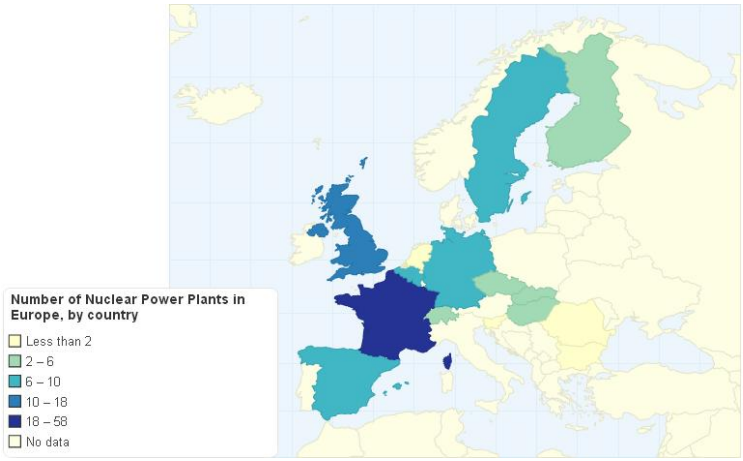

Figure 1.1: Nuclear Power Plants in Europe

Thanks to its long term and sustainable policy, Sweden ranks between the highest among EU countries in terms of share of carbon emissions: the average Swede infact, releases 5.1 tons of carbon dioxide per year into the atmosphere, compared with the EU average of 7.9 tons [6] One of the reason for this low emission rate is that about 40% of electricity in Sweden comes from nuclear power which generates a fairly negligible amount of carbon emissions

Sweden has 10 nuclear power reactors spread in three operational power plants as shown in Figure 1.2: three boiling water reactors (BWRs) are placed in Forsmark, three BWRs in Oskarshamn and one BWRs together with three power water reactors (PWRs) are working in the nation's largest power station, Ringhals Nuclear Power Plant which generates about 15 percent of Sweden's annual electricity consumption.

Sweden began its research into nuclear energy in 1947 with the establihment of the Atomic Energy Company, which originated in the ongoing military research and developement department at the Defence Institute.
In 1954 the first heavy water reactor was built in Ågesta, the second one in Marviken, which was finished but never operated due to several safety issues. Both were heavy water reactors so that the Swedish uranium could have been used without the need of an isotope enrichment; later on in the 1968 Sweden signed the Non-Proliferation Treaty, embracing the use of plutonium for its power reactor. The small implant in Ågesta, have been working and delivering heat and a little electricity to Stockholm for 20 years; it was shutted down in 1974.
The first boiling water reactor was designed and built up by thw OKG-Oskarshamns Kraftgrupp company in Oskarshamns, while the other ones were commissioned to Vattenfall, a Swedish state-owned power company which built up the nuclear im-

plants in Ringhals and Barsebäck; they also cooperated with other utilities to build the Forsmark nuclear plant, in the Uppland province.
As a result, six reactors entered commercial service in the 1970s and six in the 1980s; the implant in Barsebäck definitely closed in 2005 due to political decisions.

Figure 1.2: Nuclear Reactor in Sweden: in green are showed the operating ones and in red the implants which have been shutted down.

After the partial meltdown at the Three Mile Island Nuclear Generating Station (United States) in 1979, Swedes were called for a national referendum about the future of nuclear power there. As a result of this, it was decided in 1980 that no further nuclear power plants should be built, and that a nuclear power phase-out should be completed by 2010.
But it has not been all so simple as expected: the nuclear phase out policy has been controversial and the Swedish government has to date not produced an effective, long term energy policy with a view to dismantle its entire nuclear power program. In 2009 infact, it was banned to construct new nuclear reactors, although contruction will only be at existing sites and to replace the actual ten units. The Alliance government in a policy document can formally be said to have reversed Sweden's nuclear power phase-out policy. The document recognizes that Sweden, as noted above, heavily relies on nuclear power for its supply of electricity and that in light of climate change being a top national priority nuclear power will remain an important

source of Swedish electricity production for the foreseeable future. [1]

In the light of what has being said, the nuclear waste management and disposal constitutes an important issue in the frame of the future of the Swedish nuclear programme. In the next section an overview of the Swedish methods for the disposal of nuclear waste is presented.

1.2 Swedish Concepts for High Level Waste and Spent Fuel Disposal

Even if the the nuclear phase out policy was not successful as it was meant to be, Sweden has its nuclear waste management well in hand.
In the Nuclear Stipulation Act of 1977 the politician stated that nuclear generators are responsible for the costs of managing and disposing of spent fuel, and must provide for those costs as they go. In addition to that, utilities would not be allowed to load fuel into a new reactor before it had been shown it was possible to arrange a final storage of the waste in an absolutely safe way. Also, the law offered two alternatives for the spent nuclear fuel: reprocessing and their final disposal and final disposal of the fuel without reprocessing.
In the very same year the Swedish Nuclear Fuel and Waste Management Company (Svensk Kärnbränslehantering AB, SKB) was set up by the nuclear utilities to develop a comprehensive concept for the management and disposal of used fuel and other radioactive wastes. [5]. Since its establishment, SKB has been conducting advanced research in the area, trying to find a safe method for the three main kind of Swedes nuclear waste, which asks for different management method:

- operational waste
- decommissioning waste
- spent nuclear fuel

A schematic representation of the volumes of nuclear waste SKB will be dealing with is shown in Figure 1.3 where the estimation is made upon 40 years operation of the nuclear power plants:

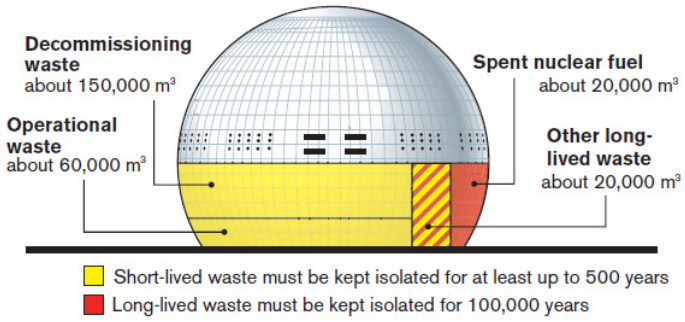

Figure 1.3: Waste volumes compared to the size of the Globen stadium in Stockholm

Operational waste constitutes the 85% of all nuclear waste. Most is low and intermediate-level waste, which requires isolation for at least 500 years: the low-level waste needs no radiation shielding and can be stored in ordinary steel-plate containers. The intermediate-level waste instead must be radiation shielded and poured into concrete or steel containers at the nuclear power plants. The decommissioning waste is constituted by scrap metal and concrete generated when nuclear power plants are dismantled. Most of this waste is low and intermediate-level, exception making for reactor rods and other core components that are classified as long-lived and must be isolated for thousands of years.
The smallest but most hazardous part of the total quantity of waste is spent nuclear fuel which must be radiation-shielded and cooled throughout handling, transportation and storage and finally isolated for 100000 years.

An overview on the method adopted in Sweden for the disposal of this kind of nuclear waste is presented in the next section.

1.2.1 SKB Concept for Spent Nuclear Fuel Disposal

Several decades of research and developement has led SKB to put forward the KBS-3 method for the final stage of spent nuclear fuel management. In this method , copper canisters with a cast iron insert containing spent nuclear fuel are sourrounded by bentonite clay and deposited at approximately 500m in groundwater saturated granitic rock as shown in Figure1.4.

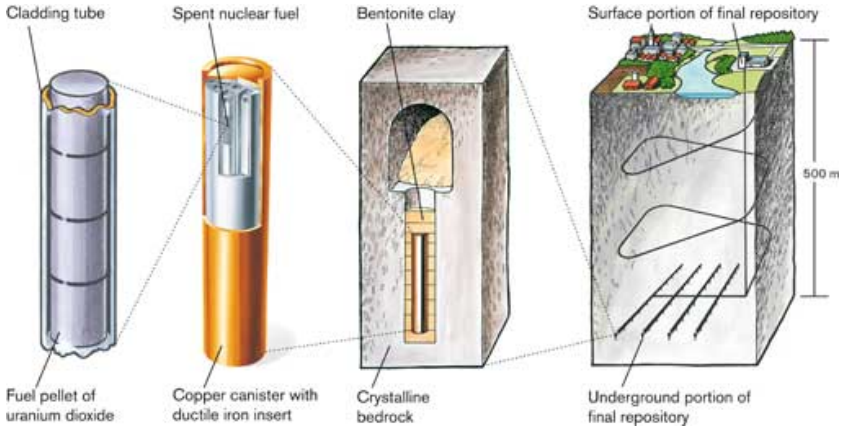

Figure 1.4: KBS-3 method for final disposal of spent nuclear fuel

Thus a multiple barrier principle is applied: the canisters isolates, the buffer seals and the rock protects. According to this, the canisters provides a corrosion and a mechanical barrier from the surroundings; the layer of bentonite clay protects the canisters against small movements in the rock, absorb water while swelling and acts as a filter trapping radionuclides. Finally, the rock protects the canisters and the buffer from mechanical damage, offers a stable chemical environment and it delays the transport of radionuclides.
This SKB's choice for the materials is based on the idea that the repository should imitate nature as closely as possible, thus the engineered barriers shall be made of naturally occurred materials that are stable in the long term in the repository environment. [7] For that purpose several studies have shown that all of the chosen materials lasted and existed for many millions of years under proper conditions. [3]

The selection of the site is the result of close to 20 years of work during which SKB has conducted surveys throughout Sweden and feasibility studies in eight municipalities. These were followed by site investigations in Forsmark and Oskarshamn between 2002 to 2007. In 2009 Forsmark was selected as the site for the final repository for Sweden's spent nuclear fuel and two years later an application was submitted to the Swedish Radiation Safety Authority and the Environmental Court. In the application they simultaneously asked for permits for the interim storage facility and an encapsulation facility which are meant to be build in Oskarshamn. A deposition permit is expected to be received in 2017 and it is believed that the mission will be completed by 2060, although recently some years of delay are forecasted.
While waiting for the authorities response, the ten reactors cited before are still in operation and SKB can count on its already existing waste handling facilities [4]:

- a *Central interim storage facility* is situated in Clab where the spent nuclear

fuel lies in underground storage pools for 30 years (Figure 1.5); in this period its radioactivity declines by 90% so it become easier to dispose of.

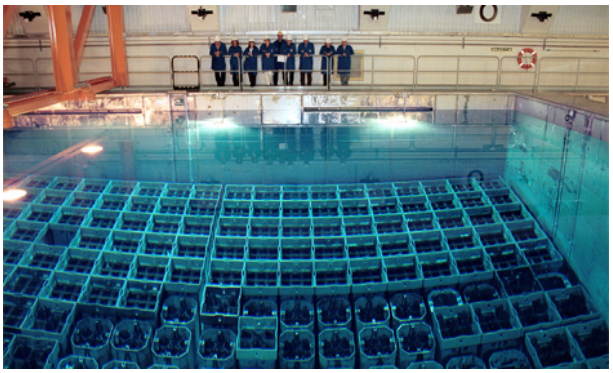

Figure 1.5: A storage pool at CLAB, the Swedish interim storage facility for spent nuclear fuel

There are actually more than 4000 tonnes of spent nuclear fuel in Clab, waiting for a final disposal site.

- a specially built ship, *ship m/s Sigyn*, which transports spent nuclear fuel to and from the various nuclear facilities.
- a *final repository for radioactive operational waste* which handles short-lived, low- and intermediate-level waste. It is an underground rock facility located at Forsmark about 50m beneath the seabed and it has been in operation since 1988.

What remain to be built are a canister factory, an encapsulation plant and - as stated above- a final repository where the spent nuclear fuel can be stored for 100 000 years, time requested for most of the radionuclides formed in the fuel to disappear. These facilities can be put into service in around 2017.

Together with those waste handling facilities SKB has to date the following well developed, cutting-edge R&D facilities: the Äspö Hard Rock Laboratory is located on an island in the archipelago next to the Oskarshamn nuclear power plant; the laboratory offers a realistic environment for different experiments and tests under the conditions that will reveal in a deep repository.
The Canister Laboratory is in the harbour of Oskarshamn and it is the centre for further developement of the encapsulation technology and related safety issues. Its primary purpose is to develop methods for welding the lid onto the copper canister and for inspecting the weld for quality assessment. [3]

The Copper Canisters

Around 12000 tonnes of spent nuclear fuel is forecasted to arise from the currently approved Swedish nuclear power programme (where the last of the 10 operating re-

actors is planned to end operation in 2045), corresponding to roughly 6000 canisters.

SKB has so far experience from full scale manufacturing of 15 complete canisters: some of them are used for experiments in the Äspö Laboratory and some of them are on display on exibitions. A summary of what has been manufactured as of 2007 is shown in Figure 1.7; for the final project 6000 canisters are needed to be produced.

Component	Method/Category	Number
Copper Tube	Rolling/Welding	13
	Extrusion	24
	Pierce and draw	10
	Forging	7
Forged lid/bottom		191
Nodular cast iron insert	BWR (Boiling Water Reactor)	46
	PWR (Pressure Water Reactor)	5
Steel lid for insert		15

Figure 1.6: Manufactured canisters by 2007

The reference design of the canister consist of a tight, 5 cm thick corrosion barrier of copper and a load-bearing insert of nodular cast iron. As shown in Figure 1.7 the sealed canister will have a total lenght of 4,835 m and a diameter of 1,050 m [7]. Depending on the kind of fuel to be stored (mainly urarium oxide fuel, MOX), the cast iron insert will be manufactured in two types, BWR and PWR, respectively for fuel coming from Boiling Water Reactors and Pressure Water Reactors.

This design will allow the canisters to comply with the following three most important safety functions [7] and [9]

- *Provide a corrosion barrier*: the canister shell must resist the corrosion to which it is exposed in the Spent Fuel Repository. The copper in the shell should therefore have a nominal thickness of 5 cm and it should be of high quality to prevent intergranular corrosion.

  The analyses in the reference evolution showed that at most a few mm of the copper shell will be corroded in one million years if the buffer's safety functions are mantained.
- *Provide a radiation barrier*: the canister must contribute to keeping the radiation on the surface below 1Gy/h
- *Withstand isostatic load*: the canister must withstand the loads associated with handling, transport and deposition. Then when the load from the groundwater pressure and the swelling of the bentonite develops, the copper will deform until it makes contact with the cast iron insert; hence, the copper must

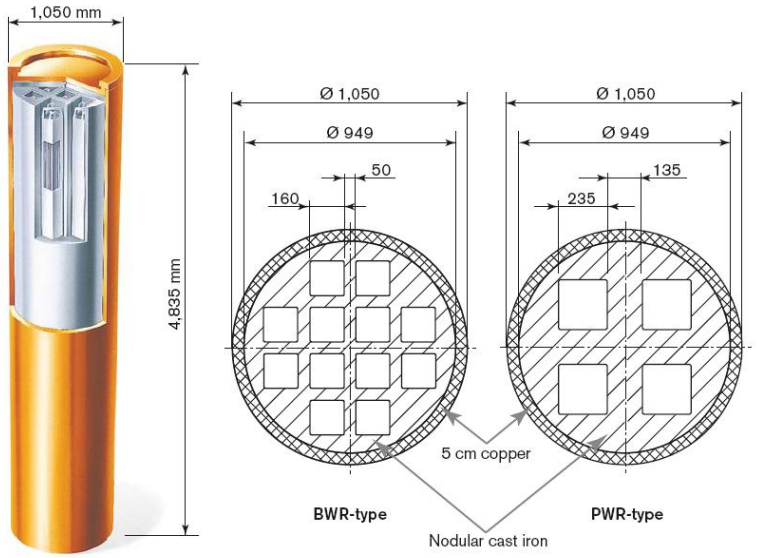

Figure 1.7: Left: the reference design with a corrosion resistant outer copper shell and a load-bearing insert of nodular cast iron. Right: cross section of insert designs of the BWR and PWR types

also possess sufficient ductility to allow straining, either plastically or by creep, when the external load against the insert deforms the canister.

- *Withstand shear load*: a rock shear movement will also result in deformation of the copper canister. The safety assessment showed that the probability of a failure due to a shear load having occurred at the end of the assessment period is 0,08 in the ensamble of 6000 canisters, with a number of pessimistic assumptions regarding both the host rock and the canisters.

The deformation of canister described above will take place at a temperature of about 100℃ caused by the fuel's heat flow: the radiation from radioactive decay infact, will interact with the materials in the fuel and the canister cavity; energy will thereby be transferred to the materials and the radiation will be attenuated. Most of the transferred energy is converted into thermal energy and heat is generated (it is estimated that the heat generation in the fuel to be of importance for a few hundred years).

The total external loading conditions which have been assessed in [9] will result in a external pressure of maximum 15 MPa which leads to plastic deformation of copper from 2.5% up to 4%. For that reason many studies have been carried out to assess the canisters capability to withstand such deformations and creep tests and modelling had been performed: both the works from Sandström in 2011 and Sandström and Yao [**?**] showed how the creep behaviour of copper is sufficiently

well understood for developing models that reproduce data from laboratory tests. In most of the creep modelling it has been assumed that the full load is applied directly and this is natural since the creep data are practically always generated with a constant applied load.
In the repository, however, the increase in the mechanical load can be expected to be slow and gradual; to simulate this situation is reasonable to use slow strain rate tensile tests (SSRT). SSRT tests have been performed on both cold deformed Cu-OFP [10] and hot worked ones [11]. These investigations cover the temperature interval from 20 to 175 ℃ and strain rates from $1 \cdot 10^{-7}$ to $0.11/s$. Also, in citeSSRTreport SSRT tests have been carried out on friction stir welded Cu-OFP.

In the present work SSRT tests are used to study the behaviour and ductility of Cu-OFP when subjected to multiaxial stress state. Before going any further, the material the canisters are made is briefly described in the next chapter.

2

Material: CU-OFP

As briefly described in Chapter 1, the material for the canister needed to respect some essential characteristics: it needed to be well characterized, easy to manufacture and available in adequate quantities. Also, it shall maintain its isolation and containment of the radioactive contents for a very long period and above all, the corrosion resistance and the mechanical endurance must be especially high. [14] Initially oxygen free high conductivity copper (Cu-OFHC) has been considered as a candidate material thanks to its considerable thermodynamic stability in reducing ground water. However, Cu-OFHC showed inadequate creep ductility, and for this reason, two candidates were chosen: oxygen free copper with 30-60 ppm phosphorus (Cu-OFP), and pure copper with 0.1% silver. The first one was expected to give the least negative influence on the corrosion properties and it was then selected. In addition to that, the cost of Cu-OFP was essentially lower than that of Cu-0.1%Ag.

In the following sections a short overview on the material which has been used in this study is given. Relations between the composition and the properties of the final component are explained.

2.1 Oxygen Free Copper

Pure copper is a natural element that has shown in nature that it can survive in comparable circumstances for millions of years. The copper's capacity for deformation and strain is also excellent and that is why it has been selected for the material of corrosion shield of the canister.

The reason for which the absence of oxygen is required for the KBS-3 project is to avoid hydrogen embrittlement, a dangerous phenomenon especially when the material is exposed to high temperatures. It has been shown that Copper in its +1 oxidation state reacts with oxygen forming Cuprite (2.1):

$$4Cu + O_2 \longrightarrow 2Cu_2O \tag{2.1}$$

and when in the +2 oxidation state the following reaction takes place, giving Tenorite (2.2):

$$2Cu + O_2 \longrightarrow CuO \tag{2.2}$$

For that reason, in the presence of oxygen, the phase diagram shall be investigated (2.1) to understand which of the compounds is more stable depending on the temperature and oxygen content.

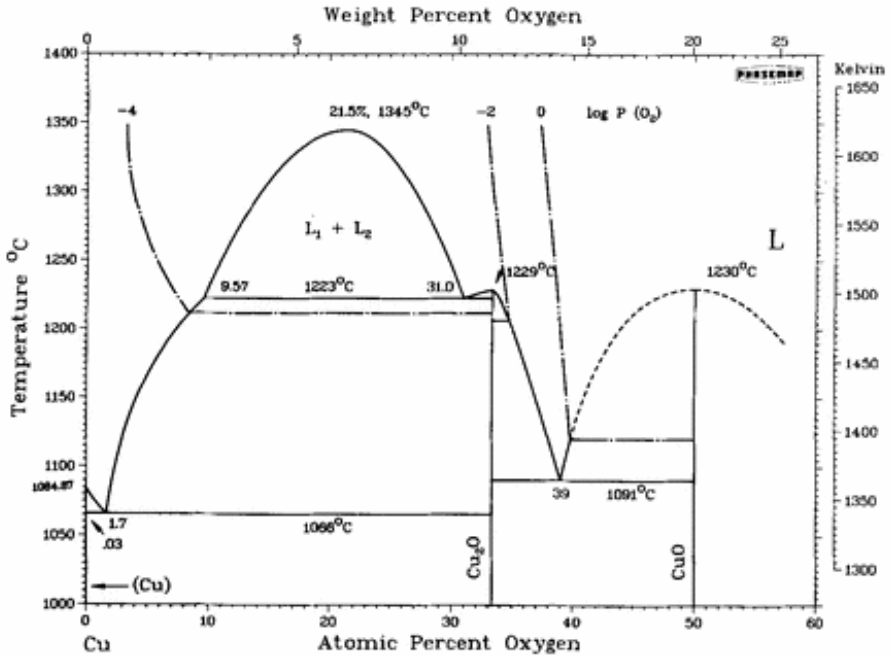

Figure 2.1: Cu-O phase diagram

From Figure 2.1 is clear how the Cuprite is stable for oxygen content lower than 34% and relatively low temperature. The problem occurs when molecular hydrogen

diffuses through the material and interacts with the cuprous oxide inclusions at the grain boundaries following the reaction 2.3

$$Cu_2O + 2H \longrightarrow 2Cu + H_2O \tag{2.3}$$

Water, hence steam is formed as pressurized bubbles at the grain boundaries which can be literally forced apart, causing grain boundary fracture and a decrease in the mechanical strength of the material.
This kind of embrittlement frequently occurs when copper is annealed and quenched in hydrogen environment and the safest solution is to severely reduce the oxygen content in the material. For that reason, the KBS-3's copper canisters must have an oxygen content lower than 5ppm.

2.2 Effect of Phosphorus on strenght properties

The presence of phosphorus plays some very important role on the oxygen free copper properties. One among the others is to limit the quantity of free oxygen, combining with it and avoiding the formation of copper oxides which are potential cause for hydrogen embrittlement as explained in the previous section.

The effect of phosphorus on copper's mechanical properties, in particular on creep ductility and creep strength has been studied for years and in the work of Sandström and Andersson[11] it is well explained and estimated: in copper the phosphorus atoms are in solid solution and since they are 16.5% larger than the host atoms , they give rise to a local stress fields that interact with those of the dislocations, impeding their motion and causing an increase in strength of the material. This mechanism is called solute hardening effect.
In [11] the solid solution hardening of 50 wt ppm phosphorus in copper was estimated using the Labush-Nabarro's model which express the increase in the yield strength as shown in equation 2.4

$$\Delta R_{p0.2} = K_{LN} \cdot \varepsilon_b^{4/3} \cdot c^{2/3} \tag{2.4}$$

where K_{LN} is a costant, ε_b is the lattice misfit parameter of phosphorus in copper and c is the atomic fraction of the solute. It was computed for the $\Delta R_{p0.2}$ to be between 0.7 and 0.8 MPa, which is a small increase in the yield strength but consistent with the measured properties with and without phosphorus.

While exerting a small influence on the tensile properties, the creep properties are strongly changed: this is because the solid solution can influence the climb movement of the dislocations which controls the rate of high temperature creep. The solute requires the dislocation an additional time to pass over it, hence its strain field reduces the climb rate.

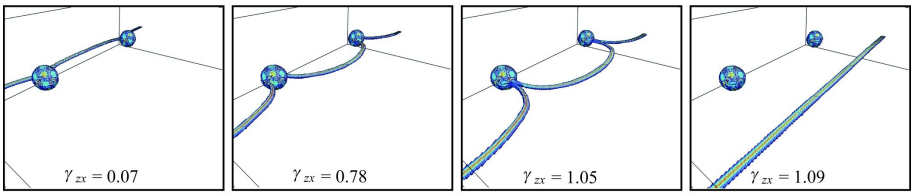

Figure 2.2: Dislocation line passing solute's particles

As schematically shown for a line dislocation in Figure 2.2, for a dislocation to move it must break away from the solute cloud. This requires an additional stress that is called the break stress. This stress for unpinning a dislocation from the P-atoms, explains the influence of phosphorous on the creep properties.

3

Creep and SSRT Tests

As planned in the KBS-3 project, the copper canisters object of this study will gradually be exposed to an external pressure of about 15 MPa due to the hydrostatic pressure from a 500 m water pillar and the swelling pressure from the surrounding bentonite clay.
It is well established that plastic deformation in stress-strain tests at constant strain rate (SSRT) and strain-time tests at constant load (creep) represents the same mechanism. In spite of this, the two types of tests are generally described with two different models which are here described.

3.1 Creep

One of the most critical factors determining the structural integrity of elevated temperature components is their creep behavior. Creep at high temperature can lead to micro cracking and ultimate fracture and, therefore, is one of the main mechanisms that limits the component life.
Creep properties are generally determined by means of a test in which a constant load is applied to a specimen and the resulting strain is recorded as a function of time.

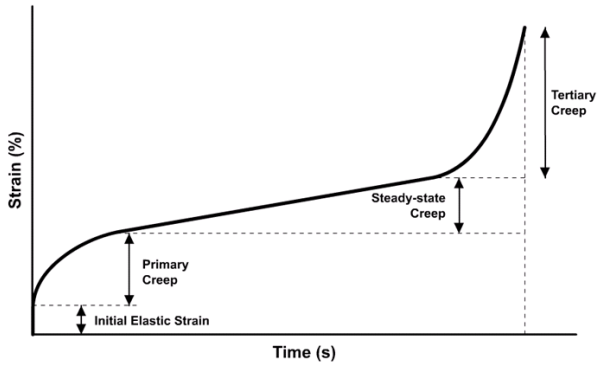

Figure 3.1: Typical creep curve

In Figure 3.1 a typical creep curve is shown: after the initial instantaneous strain, a decelerating strain rate stage (transient primary creep) leads to a steady minimum creep rate (MCR), which is finally followed by an accelerating stage (tertiary creep) that ends to fracture at a rupture time t_R.
During primary creep, the decreasing slope of the creep curve is attributed to strain hardening. Secondary stage creep is explained in terms of a balance between strain hardening, softening, and damage processes, resulting in a nearly constant creep rate. The tertiary stage is attributed to the appereance of internal and external damage processes coupled with softening processes, resulting in a decrease in the resistance to load or a significant increase in the net sectional stress.

Over the past several decades, a range of methods have been developed to predict and evaluate material's creep resistance. The most widely used methods include constitutive equations and parametric correlations.

3.1.1 Creep in copper

The placement of waste package is carried out in a depository 500 m below the ground. Creep in copper canisters tends to begin when the clay engorges by absorbing water from the surrounding or it can occur when the canister is sheared during earthquake. Behaviour of creep can be explained using power law relation at low stress and very high temperature. On the contrary, the power law relation does not hold good for the behaviour of creep at low temperature and high stress. The following equation represents the steady-state rate of pure metals [15]

$$\varepsilon = A\left(\frac{DbG}{Tk}\right)\left(\frac{\sigma}{G}\right)n \tag{3.1}$$

where b is the Burger vector, A is a fitting parameter, n is a dimentionless

constant which increases with increasing stress and decreasing temperature; D is the self-diffusion coefficient, G the shear modulus and k the Boltzmann's constant.

Atomic diffusion and dislocation motion drives the creep mechanism present in crystalline solids. Each process has its own crucial role for particular limits of stress and temperature and for different materials. For example diffusion creep is essential at fine grain size, high temperatures and low stresses. Dislocation creep instead, which includes the interaction sliding or dislocation motion coupled with stationary dislocations, plays an important role in crystalline materials.
From the equation 3.1 one can see how movement of dislocation is dependent on the applied stresses which is directly proportional to the solid's elastic modulus. Elastic modulus infact, adds a temperature dependency to the equation.
Vacancy diffusion controls the dislocation climb rate in the lattice intermediary temperatures ranging from $0.4 - 0.7 \cdot Tm$. On the other hand, at lower temperatures pipe diffusion along dislocation cores turn out to be a dominating diffusion process at lower temperatures. These are termed as high temperature climb and low temperature climb respectively. Activation energy which is affected by the diffusion process is drastically lower for pipe diffusion than volume diffusion.
The transition for P-free copper occurs at around $100Mpa$ and 160℃ whereas the transition for P-doped Cu is believed to take place at higher temperatures. In the above mentioned equation, n which is the value of dimensionless constant usually increases with increasing stress and decreasing temperature. The measurement of n values for P-doped copper was carried out by Andersson, Seitisleam and Sandström ([**?**]) which in fact ranges from 35 to 73 at 175℃. Therefore same wise like steel, copper's stress exponent increases with decreasing temperature and is in the range of 50-100.

3.1.2 Creep Testing

Creep is an important design factor for the components which are subjected to stresses at high temperature. Creep deformation and the material's rupture behaviour are infact used to calculate the material's strength and lifetime.
The material's creep behaviour is usually studied under uniaxial loading tests, which are conducted at constant temperature and under constant dead load. Strain is calculated as a function of time and tests continue until failure or until they are interrupted after a specific time. Creep curves like the one shown in Figure 3.1 are obtained which shape is influenced by the mutual balance of many factors; the following three play a critical role:

- strain hardening;

- softening process like strain softening, re-crystallization and precipitate over aging;
- damaging processes like specimen necking, cracking and cavitations.

Creep rate is decreased by the strain hardening while its increase is due to the latter two factors. In the curve's primary stage infact, the decreasing slope is the result of the hardening of strain. A balance between softening, strain hardening and damaging processes results in an approximately constant creep rate in the secondary-phase in the creep curve. Finally, in the tertiary phase, external and internal damage processes decreases the resistance to the applied load until fracture.
Equation 3.1 represent the steady state creep rate of pure metals when applying low and intermediate stresses; in [**?**] it was found to be independent from the temperature when the exponent n is calculated for the tensile tests. Acceptable agreement between the two testing technique is of utmost importance for the comparative analysis of tensile and creep data.

3.2 Slow Strain Rate Tensile Tests

As mentioned before, in the work of Sandström and Yao [**?**] it was confirmed that ordinary creep test and slow strain rate tensile test give consistent information, especially in the secondary creep stage. Also, it was shown that tensile tests results are within the scatter band of the creep data and nearly the same curve's slopes were found. The SSRT is therefore an alternative to the ordinary creep test, with the advantage of the starting phase is much more controlled than in a creep test, so it can be more easily modelled.

In the slow strain rate tensile tests which were performed in the present work, the load was varied to mantain a constant extension rate. The important characteristic of these tests infact, is that the strain rate is low, namely $10^{-6}s^{-1}$ and $10^{-7}s^{-1}$. The assimilated data were used to plot stress-strain diagram: in Figure 3.2 a general shape of a $\sigma - \varepsilon$ curve is shown.

Parameters like the ultimate tensile strength and yield strength are used to define the curve. The stress-strain diagram can be schematized as composed by two parts: elastic and plastic region. The stress is directly proportional to the strain in the first region and when it tends to a particular value, the yield stress, the material starts yielding and deforms permanently.
The yield point is usually determined by the 0.2% offset method and the tensile strenght is defined as the stress highest value which occur after the yield point.
Due to the material's work hardening, an increasing load between the yield point

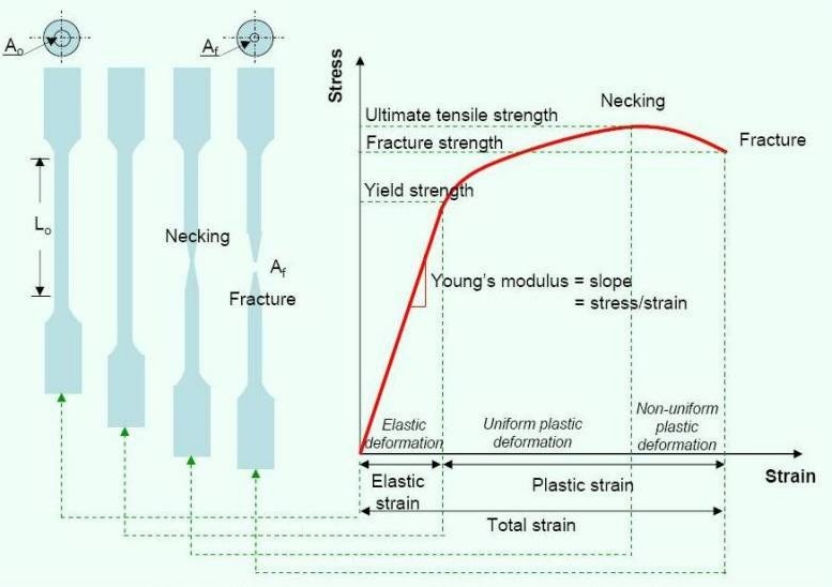

Figure 3.2: Shape of ductile specimen at various stages of testing

and the ultimate strength is required: up to the UTS the sample has elongated and reduced its cross section uniformly along the gauge length. At the maximum strength then it becomes dimentionally unstable because the area reduction had become too important for the strain hardening to give its effect; as a result the additional deformation is non-uniform and the testpiece starts to neck down at the point where it will eventually fracture.
Many factor can influence the shape and stresses magnitude in a given material's stress-strain curve such as temperature, strain rate, prior history of deformation, heat treatments and many more.

From a microstructural point of view the plastic deformation which occurs during a tensile test is due to the climb and glide of dislocations along the crystallographic planes.

3.3 Notched bars and the multiaxial stress state

The mechanism of ductile fracture is of high significance in characterizing KBS-3 copper canisters against plastic collapse and fracture. Ductility characterizes the material capability to plastically deform and the deep knowledge of this parameter is required for such a delicate issue as the spent nuclear fuel containment.
What makes ductility difficult to quantify is that it not only changes with temperature but also with the stress state.

Also, it is well known that creep failures often initiate at sites of stress concentration where a triaxial tensile stress state exist; than the developed actual stress state

will depend upon the applied loading conditions and the local geometrical configuration. The notched bar tensile test is therefore the most straightforward experimental procedure [19]. Also, a wide range of stress states can be generated across the notch throat by altering the notch profile. Geometries based on the Bridgman notch are useful for this purpose.
In Figure 3.3 the geometry of Bridgman's semicircular notches are shown: in a specimen of circular cross section with diameter D they are characterized by an initial notch root radius r_{n0} and an initial diameter of the testpiece at the notch plane (throat)d_{n0} [19]. The ratio between the radius of the specimen at the base of the notch $a = \frac{d_{n0}}{2}$ and the notch root radius $r_{n0} = R$ is defined as notch acuity.

$$NotchAcuity = \frac{d_{n0}}{2R} = \frac{a}{R}$$

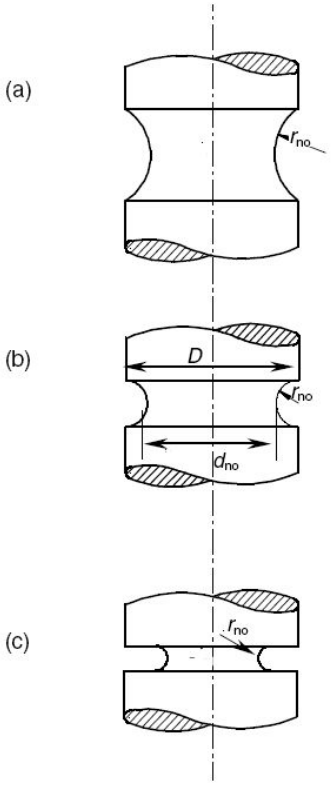

Figure 3.3: Bridgman semicircular notches profiles with different notch acuity. Notch acuity and sharpness increase from a) to c)

The stress distribution which developes during a tensile test across a notch throat is sensitive to the material properties. Initially, on loading, an elastic or elastic plus plastic stress field will be generated. With time, stress redistribution usually takes place, sometimes until a stationary stress state is achieved.
This can be seen in Figure 3.4 and 3.5 taken from the SKB report [17] where finite

element computations have been performed to interpret the tests for notched creep specimen.

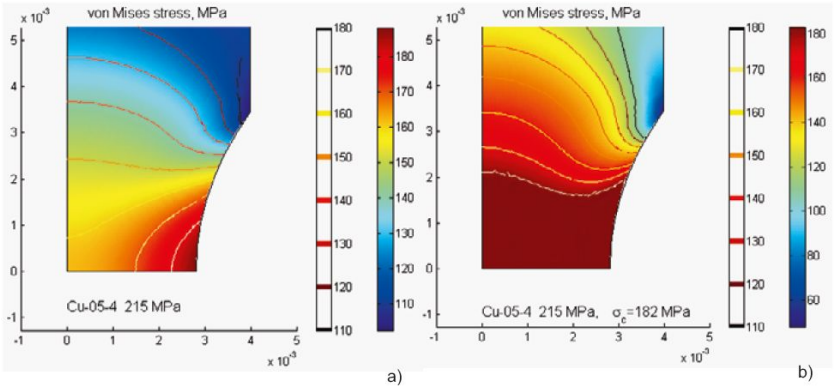

Figure 3.4: Von Mises stress distribution at the notch root for a specimen with acuity $0,5$, tested with constant load: a) directly after loading, b) after a stationary creep stress has been reached.

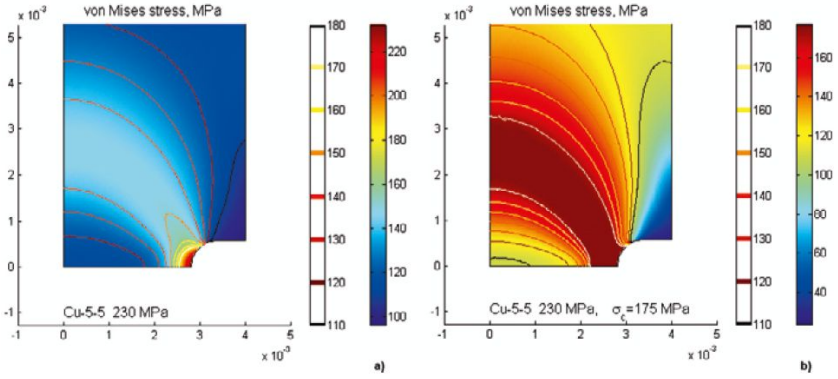

Figure 3.5: Von Mises stress distribution at the notch root for a specimen with acuity 5, tested with constant load: a) directly after loading, b) after a stationary creep stress has been reached.

In Figure 3.4 the stress distribution at an acuity 0.5 notch is shown: there was a pronounced stress concentration at the notch, marked in red. Stresses eventually redistributed and reached a stationary creep stress as shown in the right picture.
Same observations can be done when the acuity is increased from 0.5 to 5, with the difference that here the higher values of stresses are localised and confined in a smaller area. Evidently, the sharper the notch, the higher the stress concentration at the notch is. Thus, in a SSRT test the stress distribution and its developement in time is expected to be qualitatively the same.
One of the aims of the present work is to investigate the relations between the notch acuity, hence the stress distribution at the notch root, and the other testing parameter such as temperature and strain rate.

In the next chapter the experimental methods which were used for investigations on the material's behaviour under multiaxial stress state by means of SSRT tests are explained.

4

Experimental Testing

4.1 Experimental Apparatus

In the first section of this chapter the discussion is confined to the basic parts of the apparatus that were necessary to carry out the experiments: after an overview on the specimen's composition, geometry and microstructure, the tensile test machine are introduced. Also, the needed tools for the microstructural investigations and observations are briefly described. The second section is focused on the method and procedure for both the mechanical testing and the metallographic investigations.

4.1.1 SSRT Specimens

As described in Chapter 2, the test material is pure, oxygen free copper doped with 45-60 ppm of phosphorous. The exact composition is given in Table 4.1 [18]. The element that has main influence on the creep properties is phosphorous and it is in its optimal range, 50-70 ppm; no other element is likely to have a significant effect.

The test materials were taken from a side of the cylindrical body of the copper canister as shown in Figure 4.1; the tube portion was provided by Svensk Kärnbränslehantering AB.
In total 30 specimens were extracted but in this work we will consider just 10-11

Cu (%)	Ag	As	Bi	Cd	Co	Cr
99,993	13,7	1,01	0,21	<0,003	<0,006	0,2
Fe	H	Mn	Ni	O	**P**	Pb
1,1	0,30	<0,01	2	2	**45-60**	<1
S	Sb	Se	Si	Sn	Te	Zn
5	1	<1	-	<0,5	<1	<1

Table 4.1: Composition of tested material, ppm

of them, the ones who went to rupture during my stay at the Material Science Department. However, further testing are still running in the laboratory.

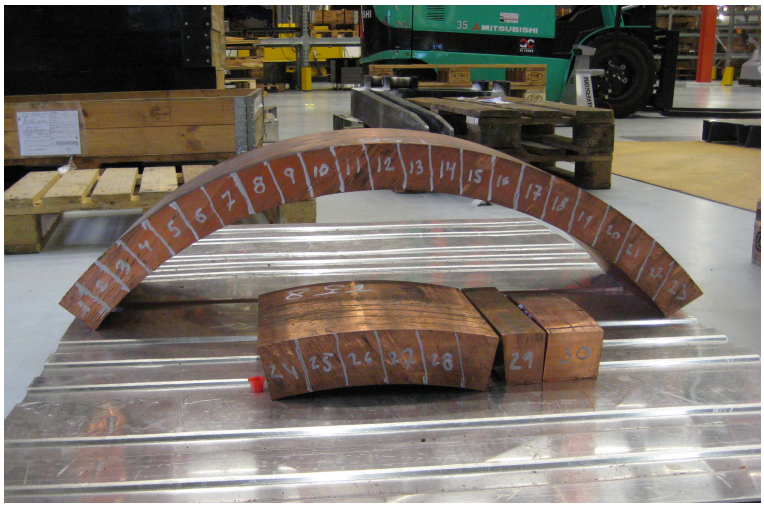

Figure 4.1: Copper canister shell from which the specimens were extracted

24 cylindrical, double notched specimens with threaded ends were manufactured. As described in Chapter 3, notched specimens are used when the effect of a multiaxial stress state on material's properties is to be investigated; therefore also 6 un-notched specimens were manufactured, to provide uniaxial stress state data for comparison and for demonstrating notch strengthening or notch weakening behaviour.
As suggested in the "A Code for Practice for Conducting notched bar creep tests and for interpreting the data" [19], Bridgman notched (semicircular) were used, since they are more suitable for determining material behaviour under triaxial stress state.

In Figure 4.2 the four kind of specimen geometry are shown. Three different notch acuities were chosen: 0.5, 2, and 5. The acuity, as explained in chapter 3, is defined as the ratio a/R, where the parameter a is the radius of the specimen at the base of the notch position and R the notch root radius. As an example the drawing

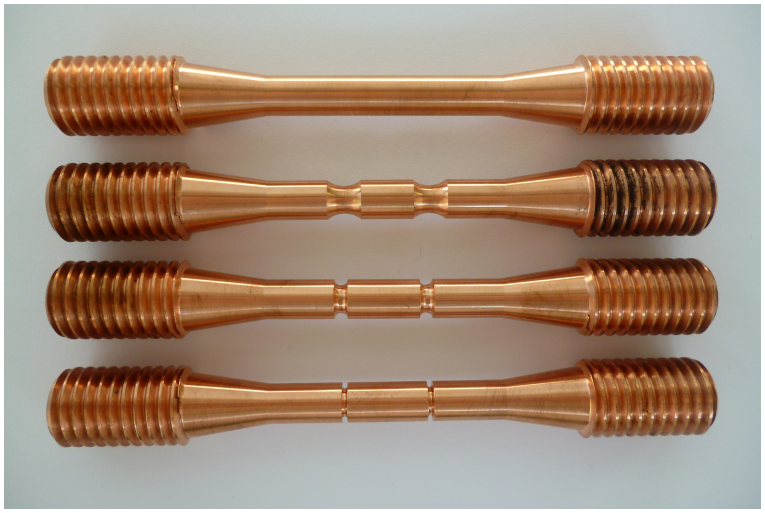

Figure 4.2: Cylindrical, double notched specimens set: from the top acuity 0, 0.5, 2 and 5

of a cylindrical, double notch specimen with acuity 5 is shown in Figure 4.3

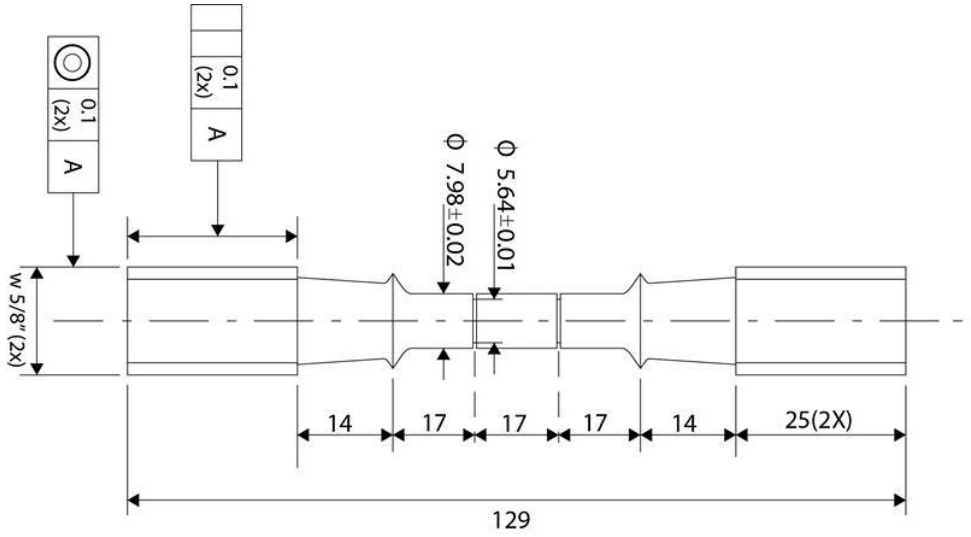

Figure 4.3: Dimension of a double notched cylindrical specimen with notch acuity 5

The specimens have a total lenght of 129 mm, a gauge lenght of 46,9 mm and a lenght without thee screw of 79 mm; the diameter at the bottom of both threaded end is 13 mm, the gross radius of the specimen is 7,98 and the net section 2a is different for each kind of acuity as is better shown in the notch detail drawings in Figure 4.4 it can be seen infact that according to the definition of the notch acuity, the larger the a/R value, the sharper the notch.

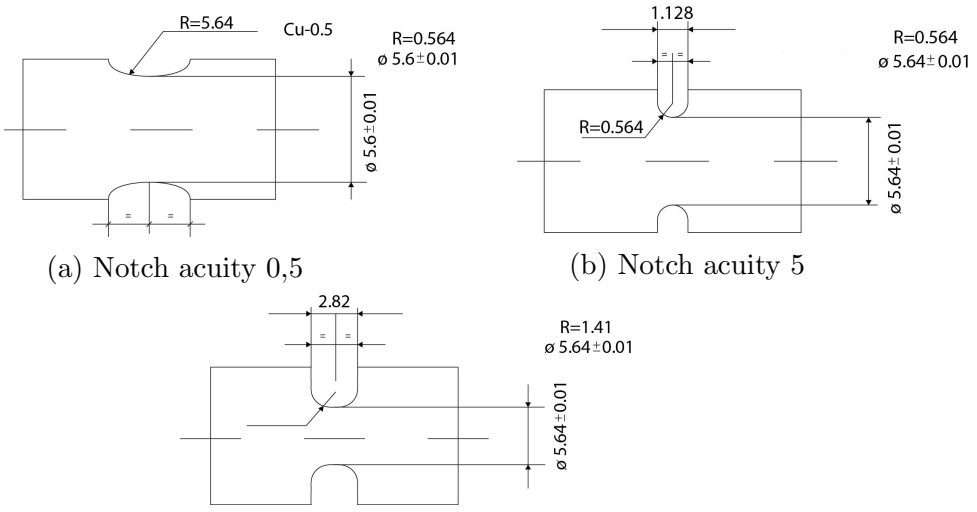

(a) Notch acuity 0,5

(b) Notch acuity 5

(c) Notch acuity 2

Figure 4.4: Drawings of the three kind of notch acuities

In Table4.5 the specimen's dimentions are summarized. Before testing each specimen dimentions have been checked with a calibrated Vernier caliper; the average dimention for each feature and group of specimen type is reported in Table 4.5 Every set of samples was verified to have dimentions which fell beneath specification's limits.

NR	ACUITY	2a	NOTCH LENGHT	GAUGE LENGHT	L WITHOUT SCREW	WHOLE LENGHT	BOTTOM Ø	Ø1	Ø2	Ø3
DESIGN DIM.	5	5,64	1,12							
	2	5,64	2,82	46,9	79	129	13	7,98	7,98	7,98
	0,5	5,6	6,65							
average	5	5,644	1,124875							
	2	5,63975	2,821375	46,965	78,30333333	129,275	12,865	7,9765	7,978533	7,9802
	0,5	5,5945	6,655375							

Figure 4.5: Designed and average specimens dimentions: the latter were calculated after 3 repeated calliper measurements.

4.1.2 Tensile Tests Machines

The mechanical testing were conducted using two electromechanical uniaxial tensile testing machines: the NT101 and the NT2005 41-E model which are respectively shown in figure 4.6b and 4.6a; both were designed by Swetest Instrument AB.

The NT101 sytem (Figure 4.6a) consist of:

- 1 electro-mechanical screw with 20 KN load cell and ±125 mm stroke distance;
- 1 oven with 250℃maximum operating temperatures;

(a) Tensile test machine NT101

(b) Tensile test machine NT2005

Figure 4.6: Electromechanical tensile test machines used for SSRT tests

- 1 extensometer of type Epsilon, HT3 type, with 50 mm gaugelenght and $\pm 25,0$mm elongation limit;
- a load and temperature regulating console;
- a computer where the WinTest™software is installed.

Prior to tests, the machine parameters were optimised for the specific test conditions and material used: these parameters include the PID values and filters. The last ones are necessary to reduce the noise contribution from the received signals.
Tests could be conducted using either the load control channel or the encoder control channel: during the tests the time, the load (KN), the stroke travel and the extensometer extension values can be recorded. Furthermore, the temperature of both the oven chamber and the specimen can be registered by two thermocouples mounted in the furnace and attached to the specimen just outside the gauge length.

The NT2005 system consist mainly of the same devices, which characteristics are slightly different, namely:

- 1 electro-mechanical screw with 50 KN load cell and ± 250 mm stroke distance;
- 1 oven with 400°Cmaximum operating temperatures;
- 1 extensometer of type Epsilon, HT2 type, with 50 mm gaugelenght and $\pm 2,50$mm elongation limit;
- a load and temperature regulating console;
- a computer where the WinTest™software is installed [20].

4.1.3 Metallography Tests Apparatus

Metallography tests were carried out both on a original testpiece and on a failed specimen. The apparatus needed for that purpose consisted on a cutting machine Struers model Accutom-5, a grinding machine model Phoenix 1000 (4.7b) and a mechanical polishing machine Phoenix 4000 (4.7a)

The grinding machine was provided with Buehler Carbimet™P240, P320, P600 and P1200 abrasive papers.
The polishing machine had adjustable rotation speed and normal force and it has been used with 2 kind of cloth and 3 different Kemet diamond paste suspention with increasing particles dimentions: 3 μ , 1μ and 0,06 μ. For each set of cloth and diamond paste an optimal combination of rotation speed and normal force was set up.

(a) Polishing machine, model Phoenix 4000

(b) Grinding machine, model Phoenix 1000

Figure 4.7: Polishing and grinding apparatus

4.2 Mechanical SSRT Tests

4.2.1 Test Plan

A total of 10 specimens has been tested and brought to rupture in the present work: 8 of them were notched, thus subjected to a multiaxial stress state in the notch region; 2 of them were un-notched, so that uniaxial data were provided for comparison.
Two were the chosen exposition temperature, 75℃and 125℃and two the strain rates: $10^{-6}s^{-1}$ and $10^{-7}s^{-1}$. Due to the large extention of time needed for each test, not every notch acuity type has been exposed to different pairs of strain rate and temperature but the test plan has been thought to cover as much various test conditions as possible. Moreover, only two were the test specimens which could have been tested with $10^{-7}s^{-1}$ strain rate, as time was limited: each of those tests infact, took around 400 hours to go to rupture.
A schematic overview of the test plan with specimen's numbering is given in Figure 4.8

ACUITY	STRAIN RATE (s^{-1})	T (°C)	SPEC.NR
0	10^{-6}	75	51
		125	50
5	10^{-6}	75	45
		125	38
	10^{-7}	75	52
2	10^{-6}	75	16
		125	42
	10^{-7}	125	19
0.5	10^{-6}	75	12
		125	17

Figure 4.8: Testing programme: for each specimen the strain rate and the exposition temperature is showed.

4.2.2 Testing Procedure

As already described in the previous section the specimens designed dimention have been checked; infact, every sample was verified to be beneath the specification limits.

The mechanical testing were conducted using the two uniaxial tensile test machines described before. The samples were mounted in the machines using the holding fixtures to ensure that the uniaxial tesile testing took place under controlled conditions. As shown in Figure 4.9 the Epsilon extensometers were carefully attached so that the grip was solidly fixed in the middle of the specimen's lenght. The NT2005 extensometer has a maximum elongation limit of 2.5 mm (5% strain), therefore it was necessary to remove it, reset it to zero and remounted when the strain got close to the above mentioned limits. This produced small discontinuities in the data which were corrected for later on.
In the NT101 machine a thermocouple was attached at one edge of the specimen with high temperature tape: in this way eventual differencies between the chamber and the specimen temperature could have been recorded.

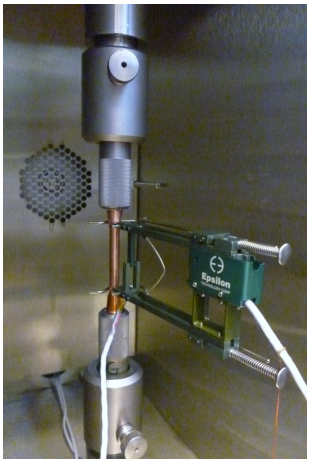

Figure 4.9: Specimen with no notch mounted on the NT101 machine

The testpieces were then heated for some minutes before the start of the test in order to homogenize the temperature distribution.
For each sample data for force, load, stroke travel, extensometer extension, time and temperature were collected by means of the WinTest software. In the program the required parameters for the tensile test were set: a ramp function with a strain rate of $4,7 \cdot 10^{-5} s^{-1}$ or $4,7 \cdot 10^{-6} mm/s$ (equivalent to $10^{-6} s^{-1}$ and $10^{-7} s^{-1}$)was defined; the number of points acquired in a time interval of 4000 s was set to be 10. Low frequency filters were chosen in order to remove noise and interference on the signal: for every recorded parameter 0,5 Hz was estimated to be a reasonable value. Also, the machines were programmed to stop if certain limit values for the load and extensometer extention were met: this has been done in order to prevent premature rupture of the specimens.

To start the test an initial load was input using the encoder control channel on the machine: values between 0,1 and 0,05 KN were necessary to put the specimen in tension within the machine's holding. In this way uneuseful time waited for the load to increase was avoided.
Each specimen was expected to go to failure in one of the two notches, were the stress concentration took place (see Chapter 3). The data recording was set to stop once the load turned back to 0 MPa, meaning the specimen went to rupture. In Figure 4.10 the failure of a notch acuity 2 is shown as an example

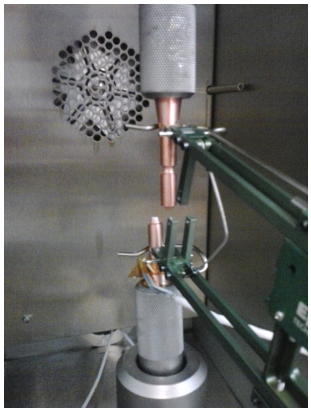

Figure 4.10: Broken specimen with notch acuity 2 on the NT101 machine

4.3 Post-Test Metallography

After testing, 2 specimen were chosen for microstructural investigation: one defective specimen (number 43), which hadn't been used for testing, provided the undeformed, original microstructure. The other one was the testpiece number 16 (Figure 4.11), which was exposed to a strain rate of $10^{-6}s^{-1}$ and a temperature of 75°C.

Figure 4.11: Broken specimen with acuity 2, exposed to $\dot{\varepsilon} = 10^{-6}s^{-1}$ and T=75°C

The first one was trasversely cutted in an arbitrary section beneath the gauge length; a cylinder was extracted and mounted in a resin holder in such a way to expose the transversal section of the specimen. It was then grinded with 4 paper, from the coarser (240p) to the finer (1200p); in each step the specimen was holded

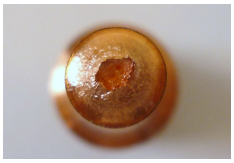

(a) Testpiece 16: broken section nr.1

(b) Testpiece 16: broken section nr.2

Figure 4.12: Specimen 16's broken sections

in the same direction and for enough time to remove the 90 degrees scratches of the previous grinding step. The specimens were thoroughly washed between each step. Three polishing step were then carried out; the mechanical head of the machine was used just for the first two stages, the ones performed with the 3μ and 1μ respectively. Because of the high ductility of the material, unwanted scratches were easy to obtain and the last polishing stage was decided to be carried out manually and with no suspension; water was used instead. The process went on until a satisfactory surface finish was reached.

The optimal etching solution for the specimens was found to be the one in [**?**] which contained:

$$40\text{g } CrO_3,\ 75\text{g } HN_4Cl,\ 50\text{ml } H_2SO_4,\ 50\text{ml } HNO_3,\ 1.900\text{ml } H_2O$$

The solution was swabbed on the specimen's surafce for less than 10 seconds: the exposure time depend on the seconds the surface takes to turn into a darker color.

From the specimen number 16 two cylinder were extracted: one containing one of the two broken section and the other containing the unbroken notch.
The longitudinal middle section was needed to be exposed for both of the testpieces so that the mode of fracture could be obtained from the broken notch, and the unfailed notch could allow the identification of the sites of damage formation. Since the particular configuration of the cutting machine didn't allow longitudinal cutting of the cilindric specimens, they have been grinded and polished until the middle longitudinal section was reached.
Then the same procedure as for the testpiece 43 was followed: when reached a sufficiently un-scratched surface trough several steps of grinding and polishing, the two specimens had been etched in the above cited solution with the same exposure time.

5

Experimental Results

In this chapter the experimental results are explained. Comparisons between stress strain curves obtained at different strain rate, temperature and notch acuity are made. The material's strength and rupture parameters are evaluated so that conclusions on the material's behaviour can be drawn.
In the last section an overview on the specimen's deformed microstructure is shown.

5.1 Stress-Strain Curves

As described in Chapter 4, values for time, load and extensometer stroke were recorded for each tested specimen and basic calculations were made to obtain both engineering and true stress strain values.
Although the true stress-true strain curves are a better representation of how the material behaves as it is being deformed, in engineering applications, where usually the task is to determine whether a load will produce acceptable values of stress and deformation, the engineering curves are preferred; their respective expressions infact, involve data which are readily available, namely the cross sectional area A_0 and the lenght L_0 of the specimen in its undeformed state. Hence, the engineering stress and strain values are used to make the final conclusion of the present work.

The equation used to calculate them from the data acquired by the tensile tests machines are shown below: the definition of the engineering stress and engineering strain were used (Equation 5.1 and 5.2)

$$\varepsilon_{eng} = \frac{\Delta L}{L_0} \tag{5.1}$$

$$\sigma_{eng} = \frac{Load}{A_0} \tag{5.2}$$

where A_0 is the initial measured area, ΔL is the extensometer stroke and L_0 the specimen's gauge lenght.
The $\sigma_{eng} - \varepsilon_{eng}$ curves are reported for each specimen in the following figures (Figures 5.1 to 5.10):

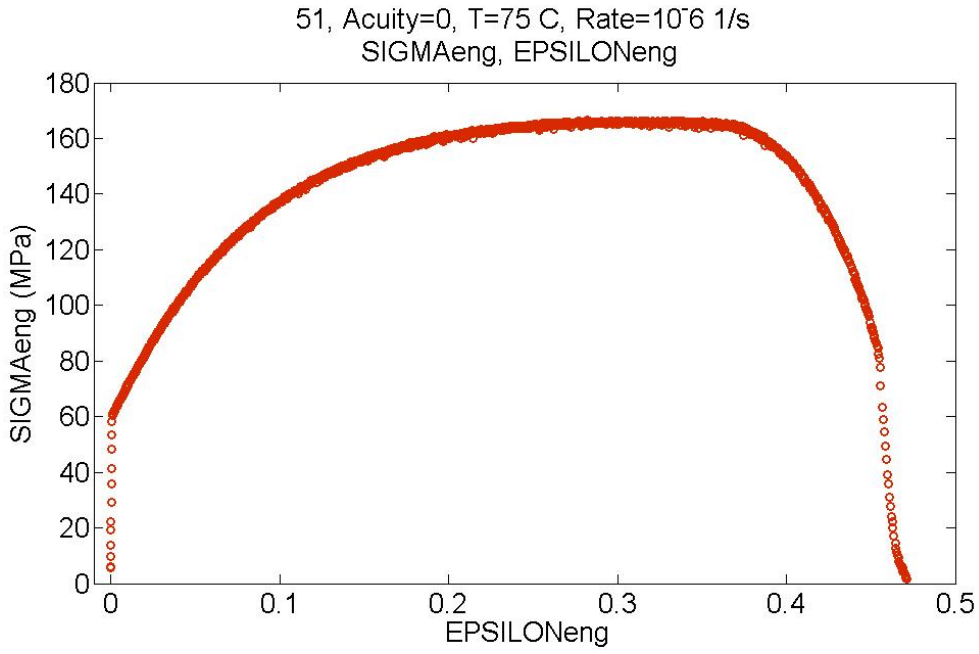

Figure 5.1: Specimen's 51 engineering curve: no notch, tested at 75°C with $10^{-6}1/s$ strain rate

The first un-notched specimen in Figure 5.1 went to failure after almost 143 h, reaching a strain to rupture of 47.2% and a maximum stress of about 167 MPa. From the curve is clearly visible the elastic trait which extends until 60 Mpa.

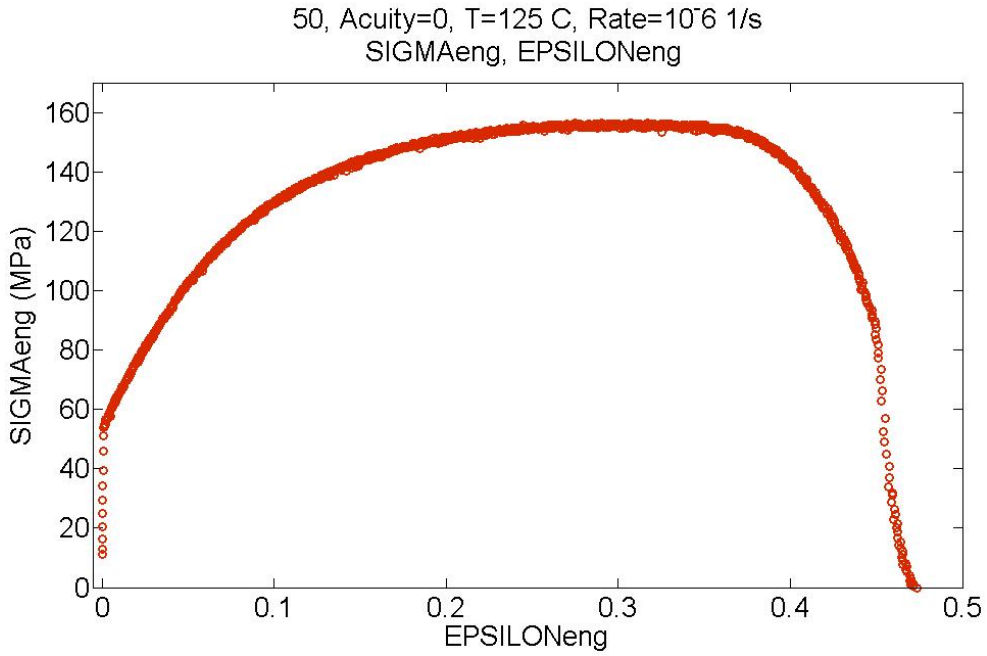

Figure 5.2: Specimen's 50 engineering curve: no notch, tested at 125℃ with $10^{-6}1/s$ strain rate

The second un-notched testpiece 5.2 was exposed to an higher temperature, namely 125℃. It reached a lower maximum stress compared to the one tested at 75℃ and it went to rupture with almost the same strain and rupture time.

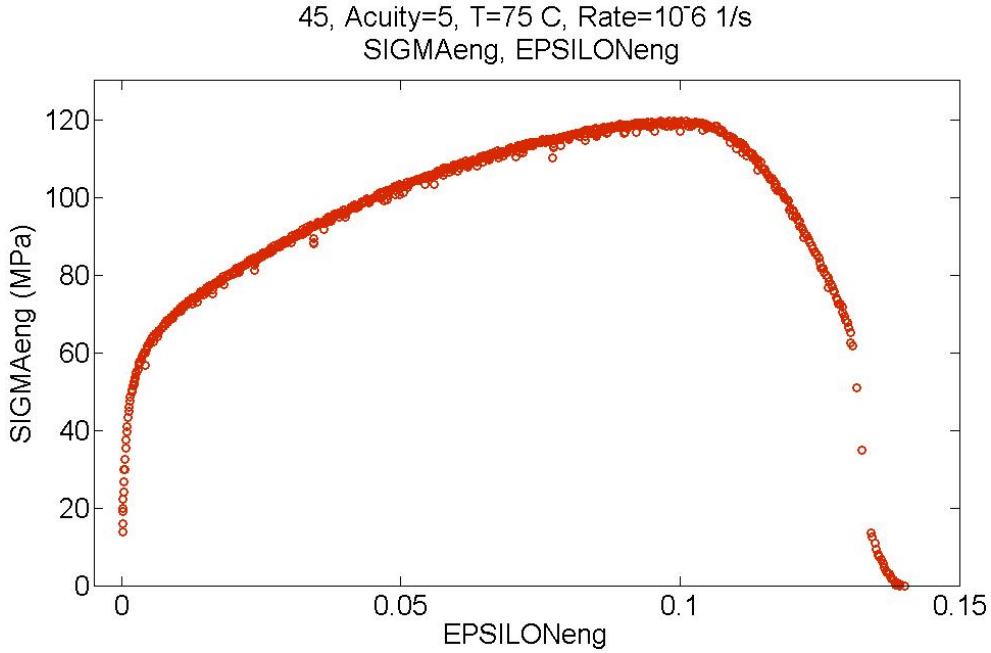

Figure 5.3: Specimen's 45 engineering curve: notch acuity 5, tested at 75℃ with $10^{-6}1/s$ strain rate

The first specimen from the acuity 5 set 5.3 was tested at 75℃ with $10^{-6}1/s$ strain rate. It comes immediately evident the effect of the notches introduction:

with a strain to rupture of about 13.9% and a maximum stress of almost 120 MPa, the specimen's strength properties are drastically reduced.

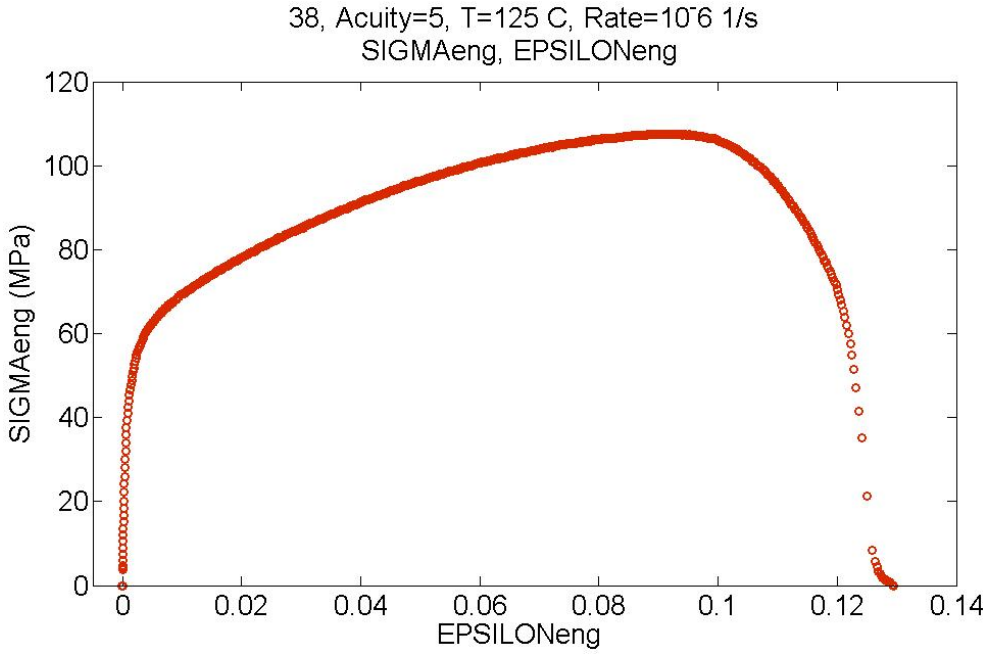

Figure 5.4: Specimen's 38 engineering curve: notch acuity 5, tested at 125℃ with $10^{-6}1/s$ strain rate

Still tested with $\dot{\varepsilon} = 10^{-6}$ but at 125℃ the testpiece 38 with acuity 5 showed a slightly lower strenght and strain to rupture if compared to the previous one, respectively of 215 MPa and 12.9% 5.4. Furthermore the shape of the stress-strain curve did not change significantly.

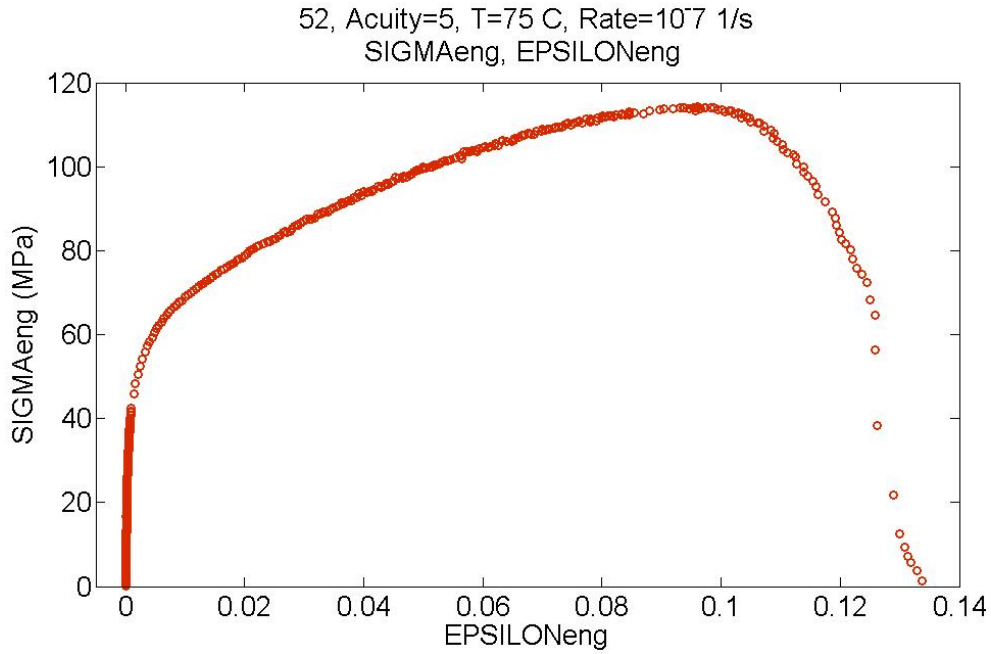

Figure 5.5: Specimen's 38 engineering curve: notch acuity 5, tested at 75°C with $10^{-7}1/s$ strain rate

The specimen 52 in Figure 5.5 was the first one to be tested with $10^{-7}1/s$ strain rate: it took 413 hours to go to rupture but other condition being equal, both the strain to failure and the σ_{max} didn't differ appreciably from the specimen tested with higher strain rate.

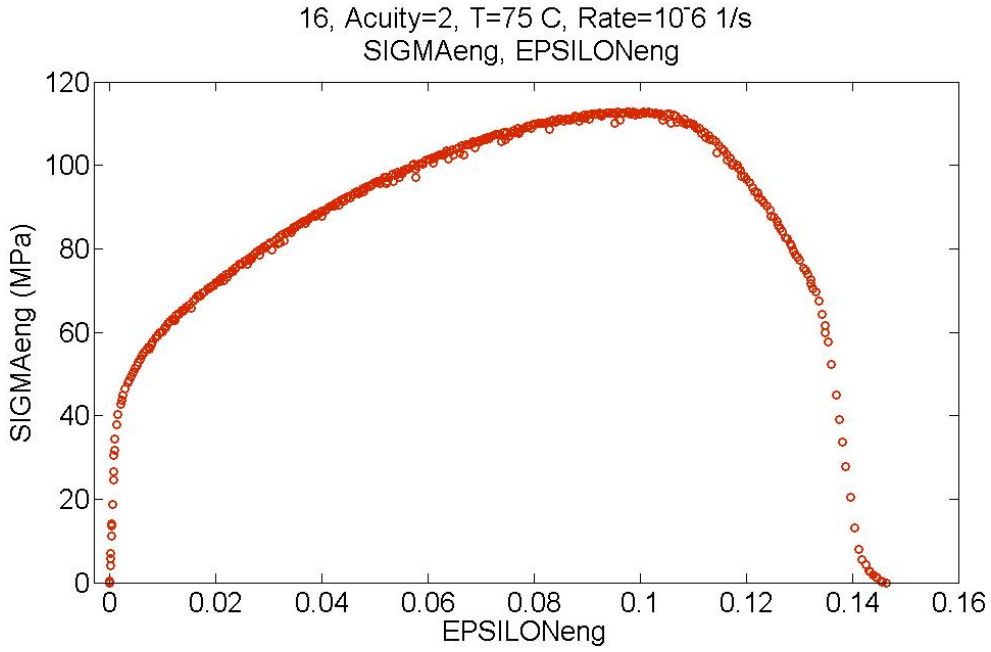

Figure 5.6: Specimen's 16 engineering curve: notch acuity 2, tested at 75°C with $10^{-6}1/s$ strain rate

In Figure 5.6 the $\sigma_{eng} - \varepsilon_{eng}$ curve of the specimen 16 is shown. It can be compared to the one obtained for the testpiece 45 as all the testing conditions were equal so that the introduction of blunter notches can be appreciated: it can be seen infact that while the maximum strength decreased of about 7 MPa, it reached an higher strain to rupture compared to both the testpiece with acuity 5. In particular its σ_{max} was 113.78, thus between the two values of the acuity 5 set. This can be better appreciate in Figure 5.11.

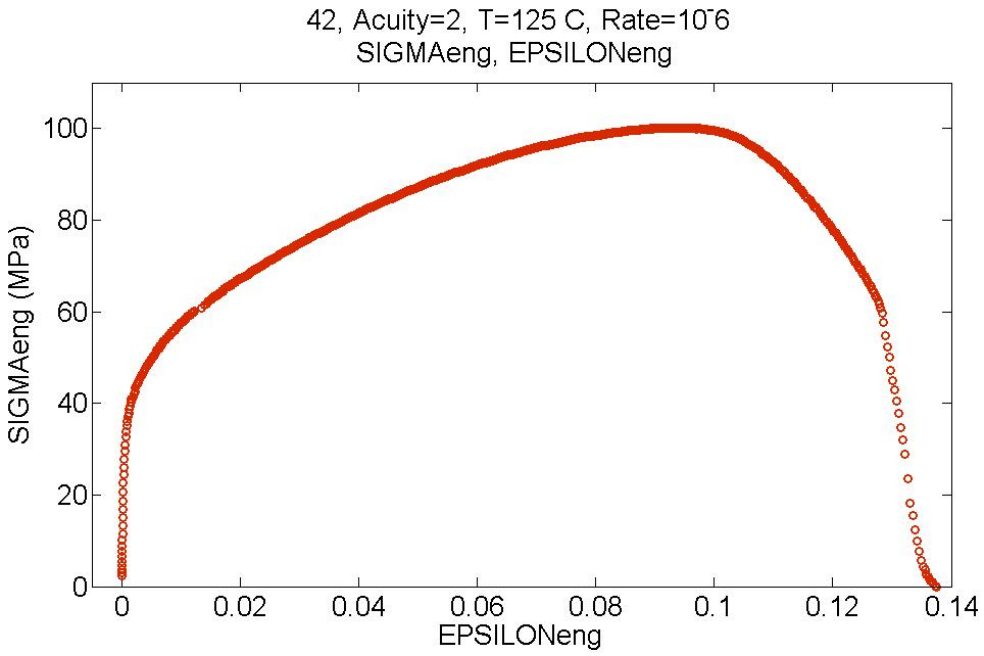

Figure 5.7: Specimen's 42 engineering curve: notch acuity 2, tested at 125℃ with $10^{-6}1/s$ strain rate

The stress-strain engineering curve of the specimen number 42 showed the same shape of the equivalent one tested at 75℃; the higher exposition temperature had infact the effect of reducing both the maximum stress and the strain to rupture.

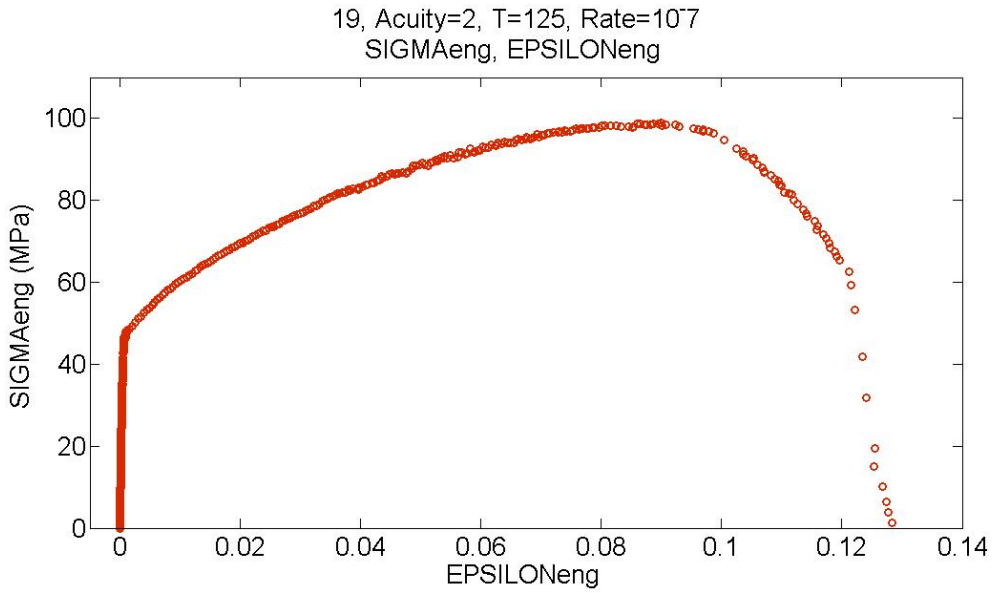

Figure 5.8: Specimen's 19 engineering curve: notch acuity 2, tested at 125°C with $10^{-7}1/s$ strain rate

The second and last specimen that have been tested with $10^{-7}1/s$ strain rate was the one shown in Figure 5.8. It went to rupture after 390 hours and a strain of 12.3%. Its maximum stress was less that 2 MPa smaller then the corrispondent specimen 52 tested at higher strain rate and other condition being equal.

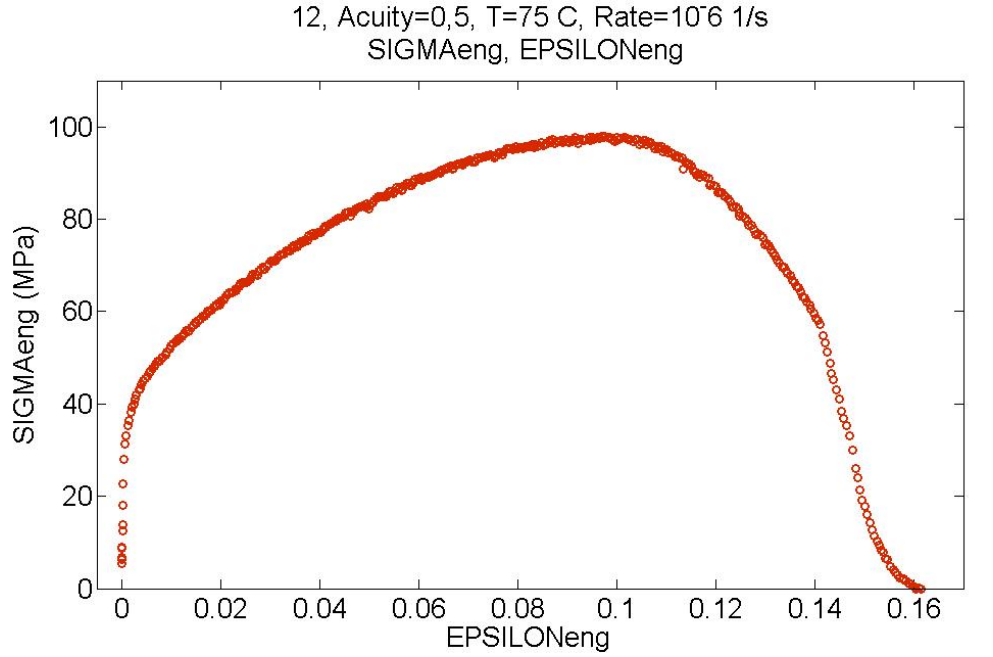

Figure 5.9: Specimen's 12 engineering curve: notch acuity 0.5, tested at 75°C with $10^{-6}1/s$ strain rate

The curves of the two specimens with the bluntest notches (acuity 0.5) are shown

in Figure 5.9 and 5.10: the first one went to rupture after almost 48 hours reaching a strain of 16% which is the higher value recorded between the notched specimens. On the other hand, its maximum stress (97.98 MPa) was the lowest between the specimens tested at 75°C.

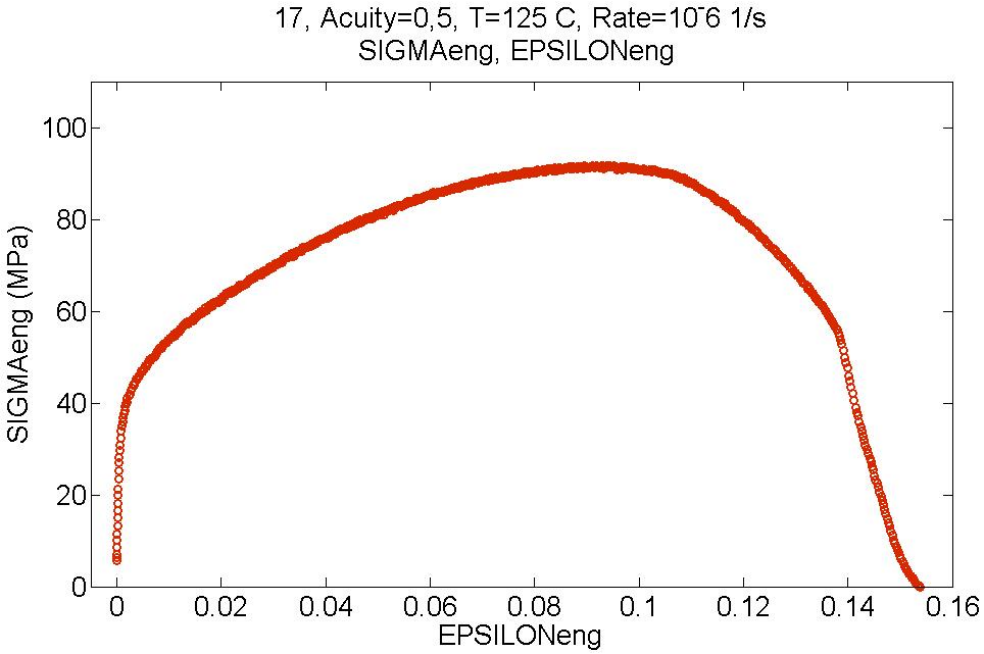

Figure 5.10: Specimen's 17 engineering curve: notch acuity 0.5, tested at 125°C with $10^{-6}1/s$ strain rate

The lowest calculated strain to rupture was the one of the testpiece 17, with notch acuity 0.5 tested at 125°C: its value is about 91.6 MPa but the strain to rupture it reached is the highest between the specimens tested at that temperature.

In figure 5.11 all the curve obtained with 10^{-6} strain rate are plotted to give an overview of the specimens geometry and testing parameter on the stress-strain curves.

True stress-strain curves Altough the engineering curves are used to extrapolate basic informations on material's strenght, the effective stress and strain values can only be found when referred to the instantaneous variations of the cross sectional area and gauge lenght. For that reason also true stress-strain curves were calculated. Basic expressions for the true strain and true stress were deduced from the engineering ones; few steps are shown below.
The engineering strain and stress are defined as:

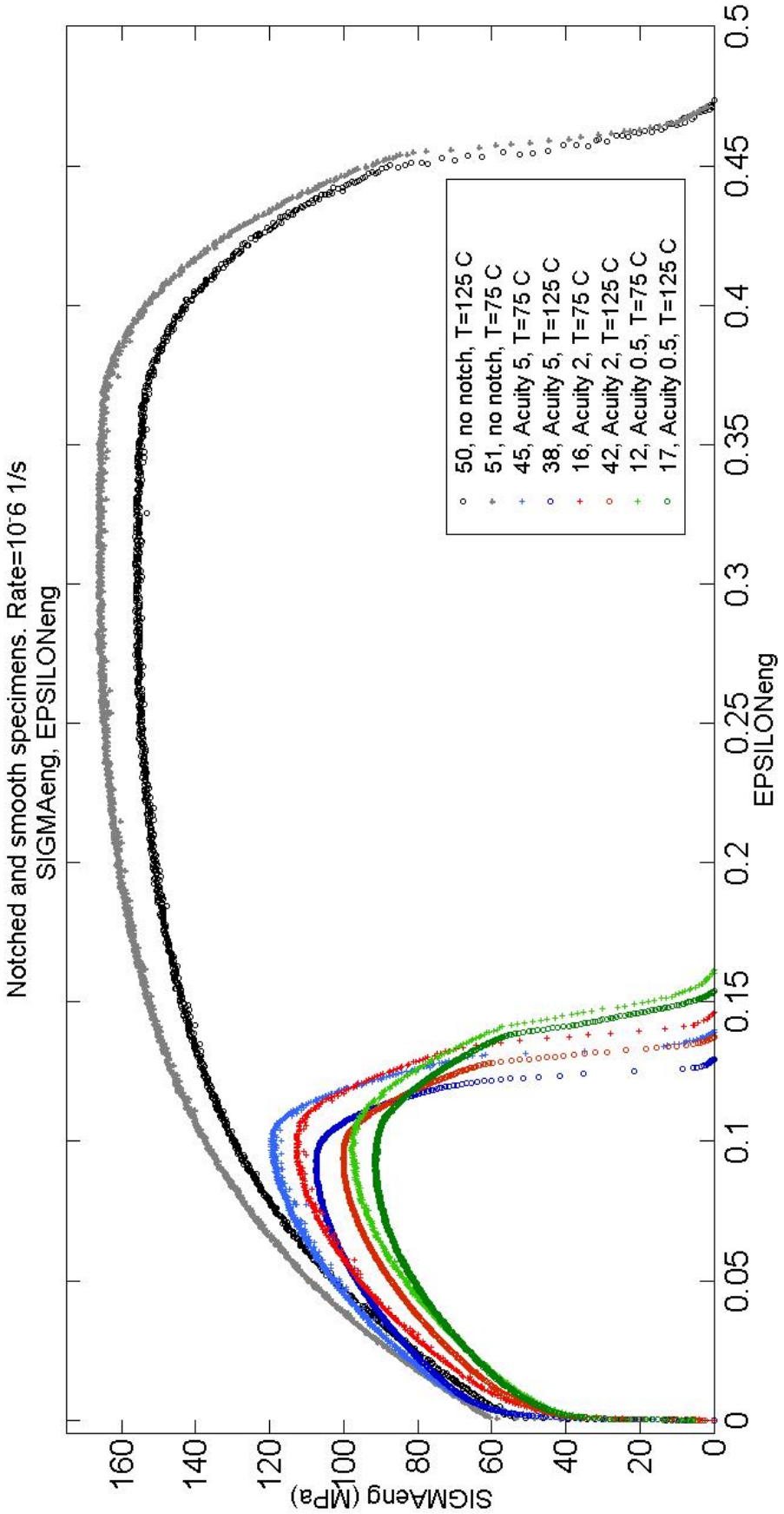

Figure 5.11: Engineering curves obtained with 10^{-6} strain rate

$$\varepsilon_{true} = \int \frac{dl}{L_0} \tag{5.3}$$

$$\sigma_{true} = \frac{Load}{A} \tag{5.4}$$

where A is the istantaneous cross sectional area or the net cross sectional area for the notched specimens.

The expression for the true strain can be modified as follows, leading to Equation 5.8 after few simple step:

$$\varepsilon_{true} = \log \frac{L}{L_0} \tag{5.5}$$

$$\varepsilon_{true} = \log \left(\frac{L_0 + \Delta L}{L_0} \right) \tag{5.6}$$

$$\varepsilon_{true} = \log 1 + \frac{\Delta L}{L_0} \tag{5.7}$$

$$\varepsilon_{true} = \log \left(1 + \varepsilon_{eng}\right) \tag{5.8}$$

The equation 5.8 is the one used to calculate the true strain values from the extensometer stroke values (L) acquired from the tensile test machine.
The expression for the true stress can be obtained from the engineering one in a similar way: thanks to the volume conservation assumption during plastic deformation (Equation 5.9), the σ_{true} can be rewritten as showed in Equation 5.11

$$A_0 \cdot L_0 = A \cdot L \tag{5.9}$$

$$\sigma_{eng} \cdot L_0 = \sigma_{true} \cdot L \tag{5.10}$$

$$\sigma_{true} = \sigma_{eng} \cdot \frac{L}{L_0} \tag{5.11}$$

Since the Equation 5.8 can be modified as $L = L_0(1 + \varepsilon_{eng})$, the final expression for the true stress can be obtained from Equation 5.12:

$$\sigma_{true} = \sigma_{eng} \cdot (1 + \varepsilon_{eng}) \tag{5.12}$$

Through equation 5.12 true stress values were directly related to the load and extensometer ones which were recorded by the tensile machine. For the calculations,

the nominal values for the initial test lenght and initial area, respectively $L_0 = 47mm$ and $A_0 = 5.64mm$ were used. For the notch acuity 0.5 set of testpiece an initial area of $5.64mm$ was taken instead.
The so calculated values for the true stress and true strain were then plotted for each specimens as shown in the next figures.

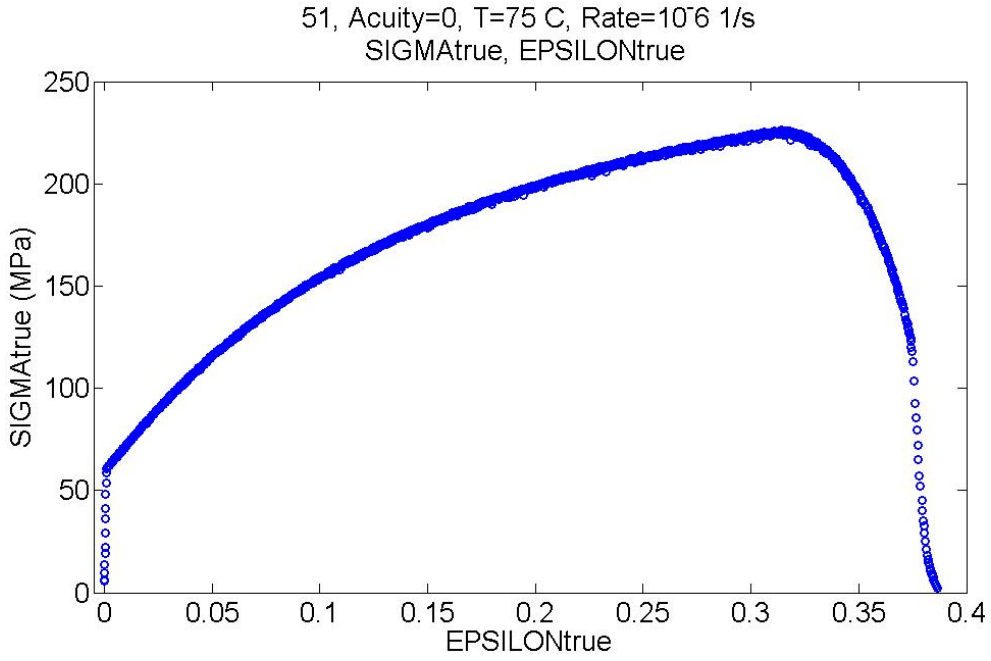

Figure 5.12: Specimen's 51 true stress-true strain curve: not notched, tested at 75°C with $10^{-6}1/s$ strain rate

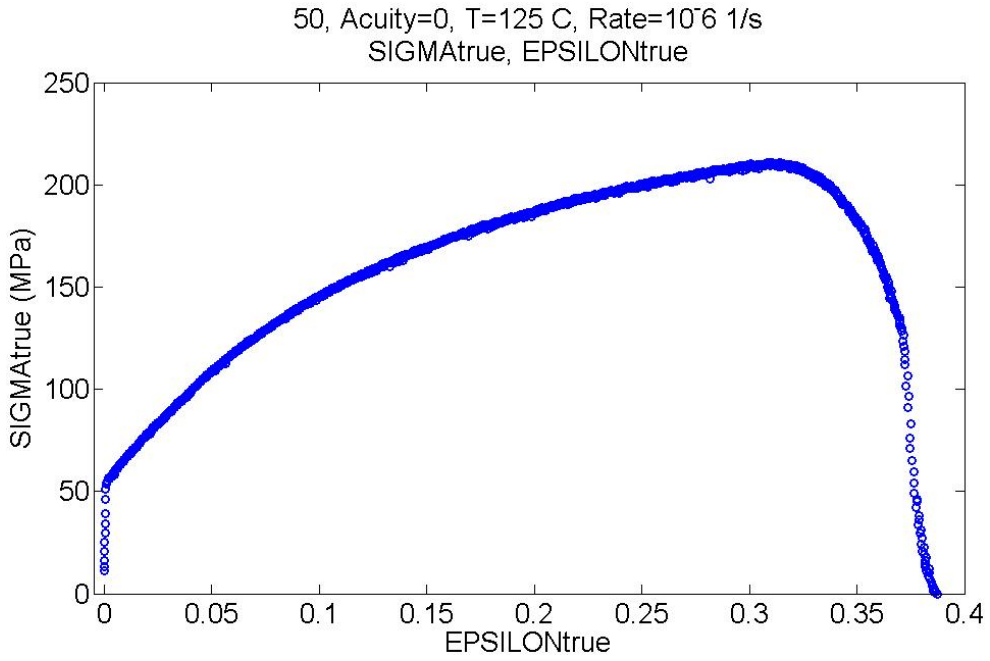

Figure 5.13: Specimen's 50 true stress-true strain curve: not notched, tested at 125°C with $10^{-6}1/s$ strain rate

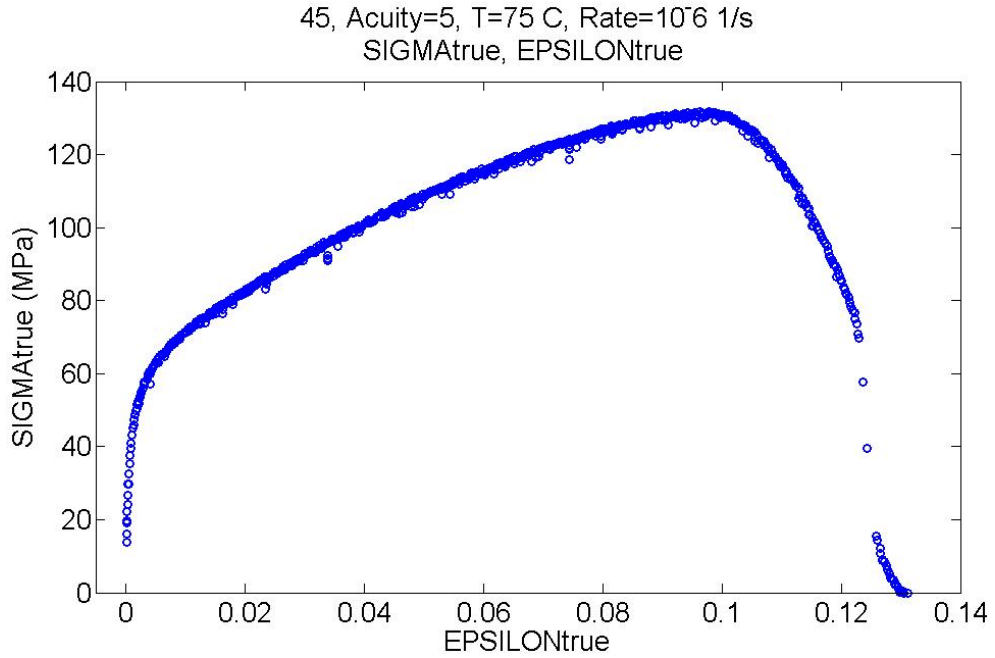

Figure 5.14: Specimen's 45 true stress-true strain curve: notch acuity 5, tested at 75°C with $10^{-6}1/s$ strain rate

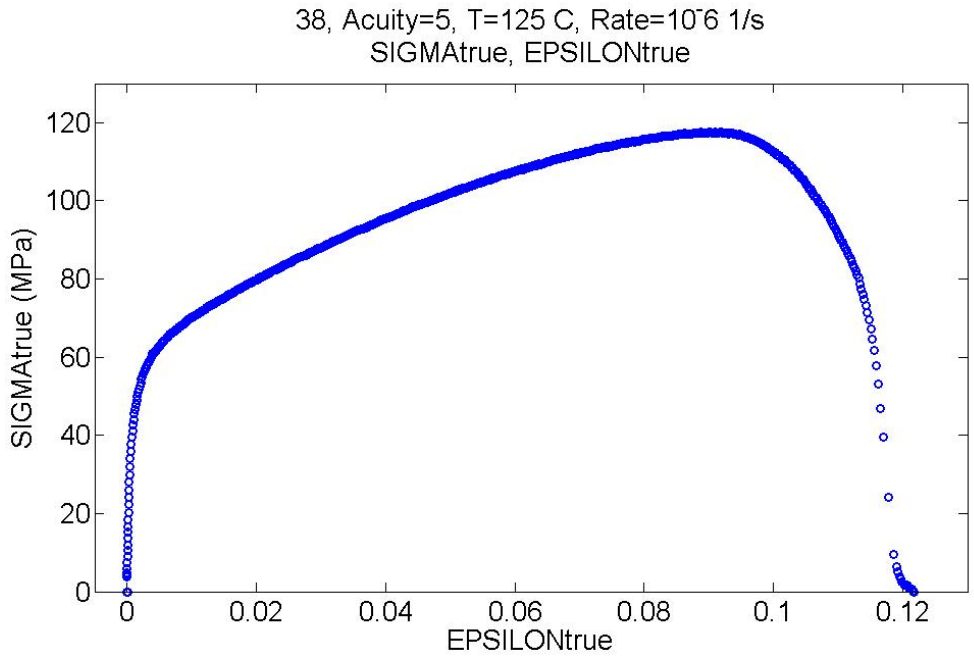

Figure 5.15: Specimen's 38 true stress-true strain curve: notch acuity 5, tested at 125°C with $10^{-6}1/s$ strain rate

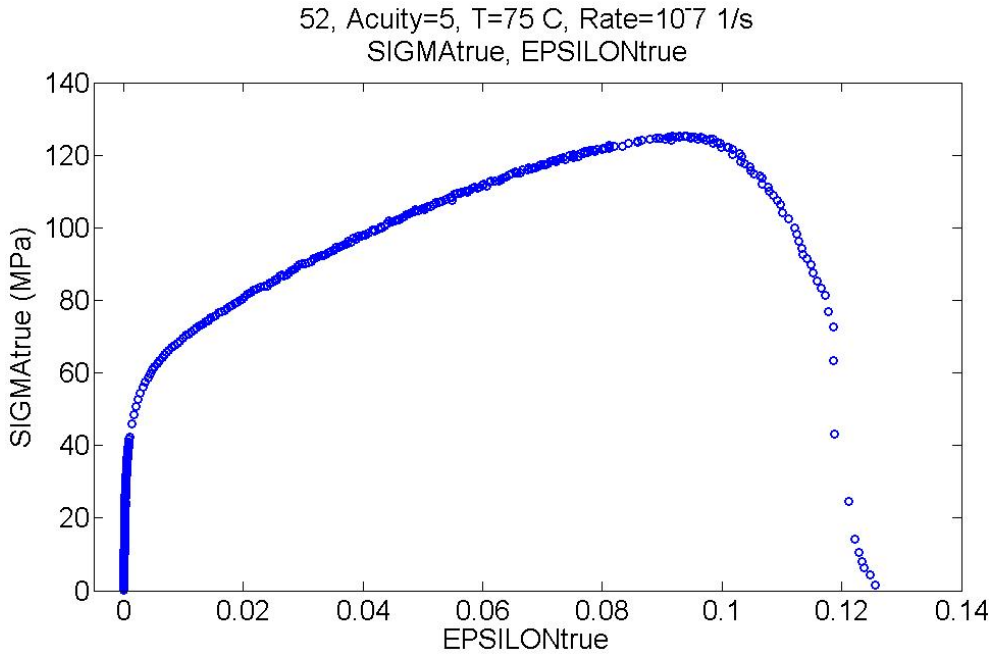

Figure 5.16: Specimen's 45 true stress-true strain curve: notch acuity 5, tested at 75°C with $10^{-7}1/s$ strain rate

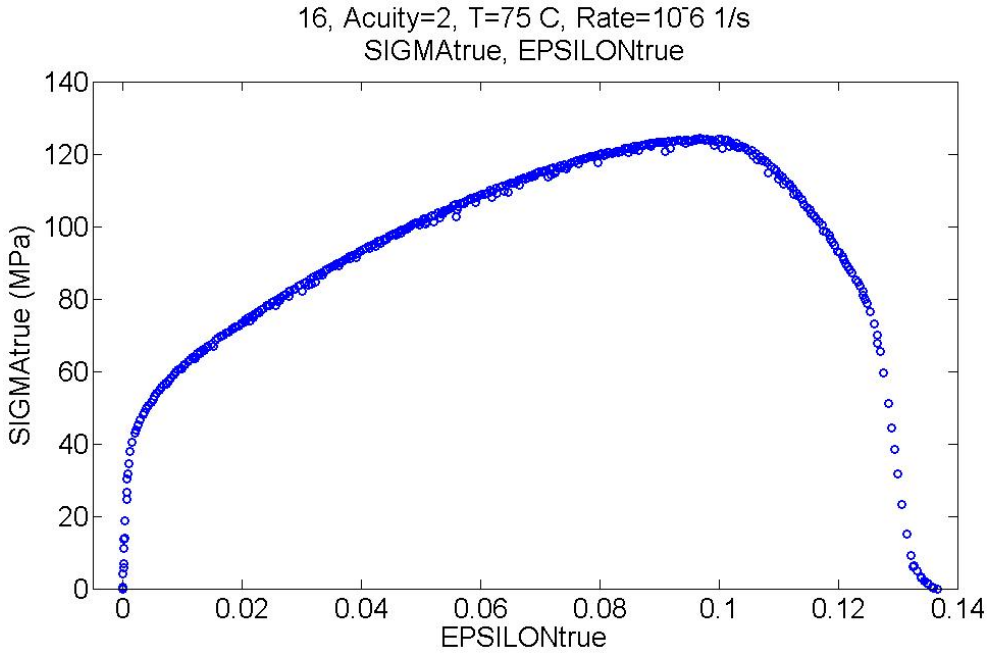

Figure 5.17: Specimen's 16 true stress-true strain curve: notch acuity 2, tested at 75℃ with $10^{-6}1/s$ strain rate

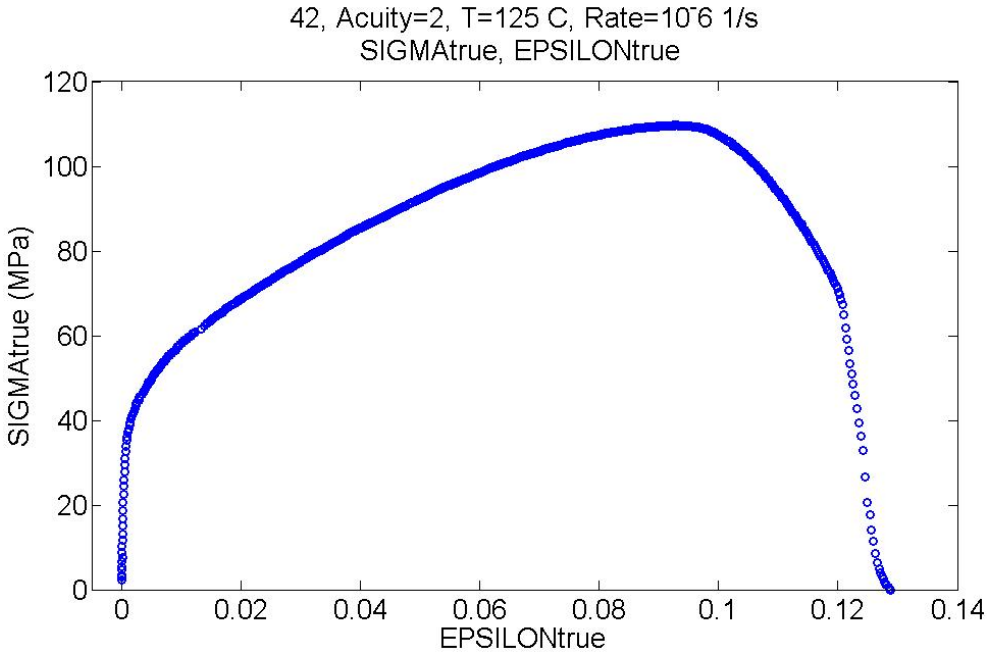

Figure 5.18: Specimen's 42 true stress-true strain curve: notch acuity 2, tested at 125℃ with $10^{-6}1/s$ strain rate

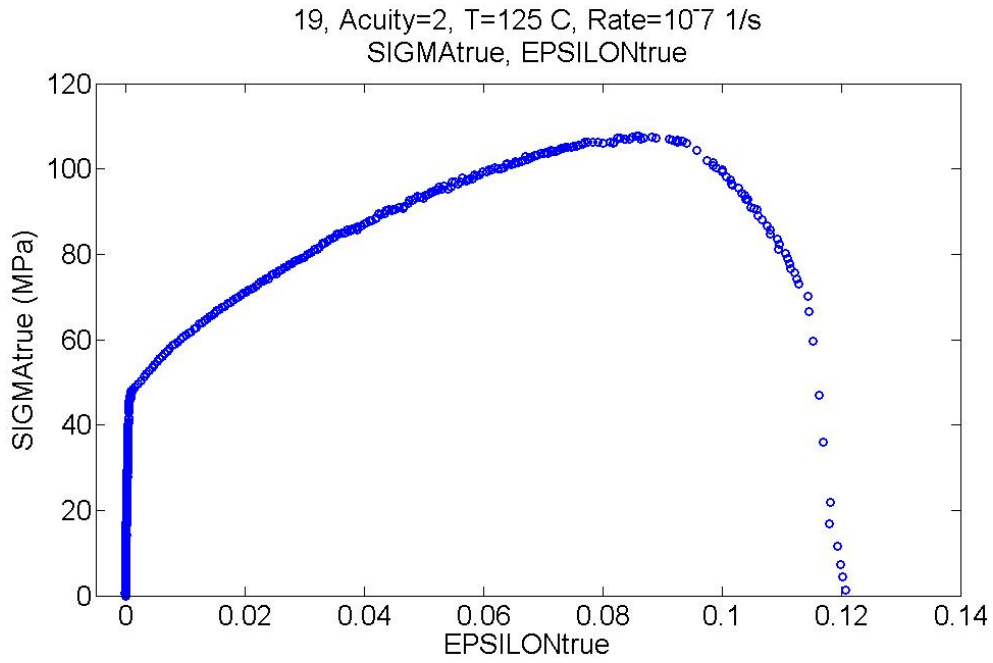

Figure 5.19: Specimen's 19 true stress-true strain curve: notch acuity 2, tested at 125°C with $10^{-7}1/s$ strain rate

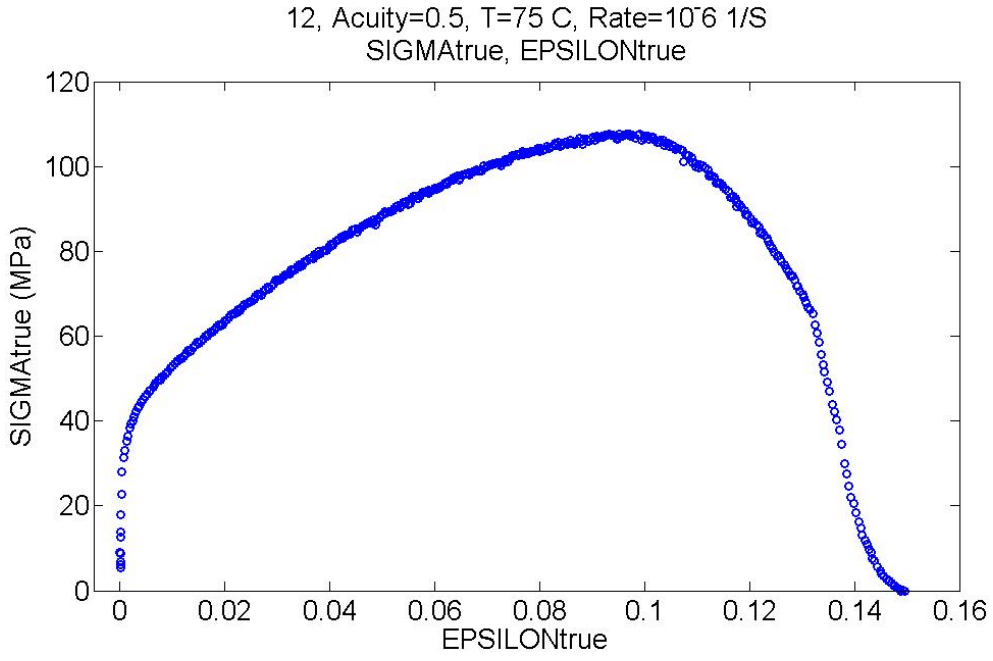

Figure 5.20: Specimen's 12 true stress-true strain curve: notch acuity 0.5, tested at 75°C with $10^{-6}1/s$ strain rate

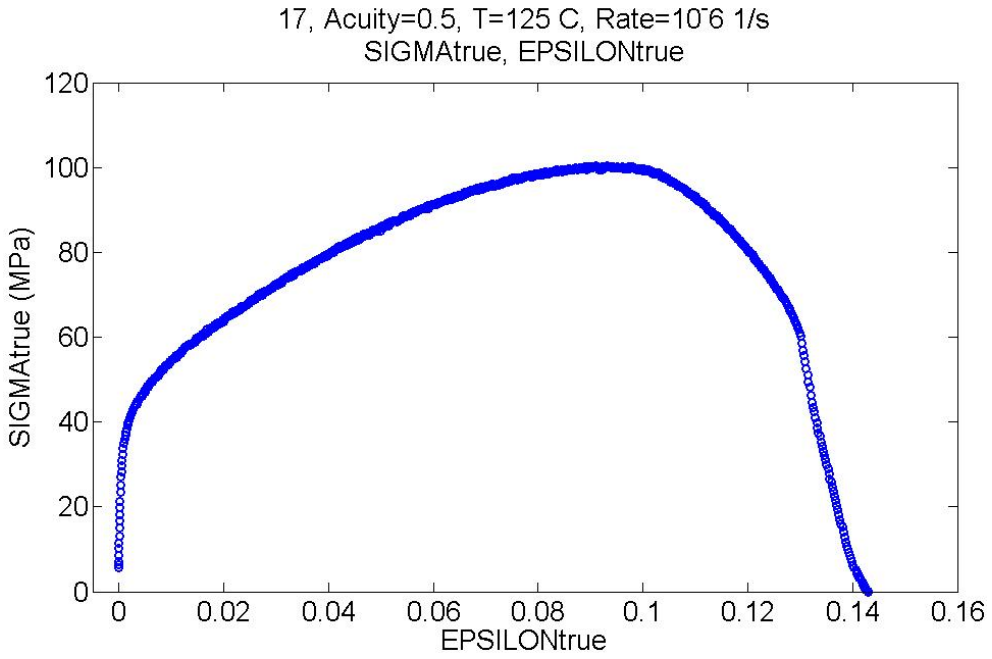

Figure 5.21: Specimen's 17 true stress-true strain curve: notch acuity 0.5, tested at 125℃ with $10^{-6}1/s$ strain rate

5.1.1 Effect of the strain rate

The effect of the strain rate on the material's behaviour can be shown with the help of the stress strain curves of the specimen number 19 (acuity 2) and 52 (acuity 5): they were exposed to 125℃ and 75℃ respectively and both loaded with a strain rate of $10^{-7}1/s$. A comparison can be made with the specimens 42 and 45 respectively since they were tested at $10^{-6}1/s$, notch acuity and exposition temperature being equal.

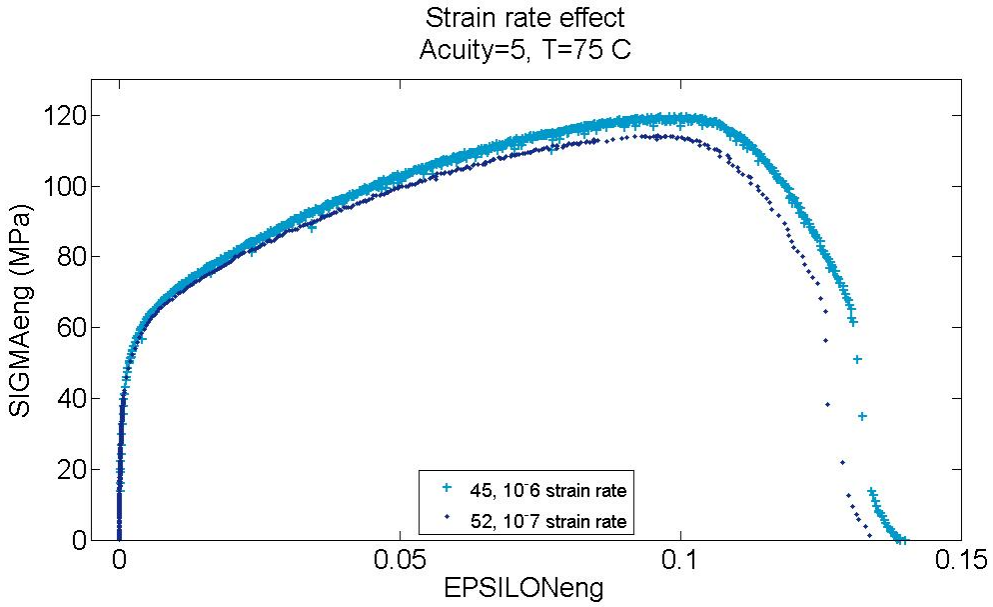

Figure 5.22: Effect of the strain rate on $\sigma - \varepsilon$ curves; the two specimens had notch acuity 5 and were both exposed to 75℃. Lighter blue colour indicates the testpiece tested with higher strain rate

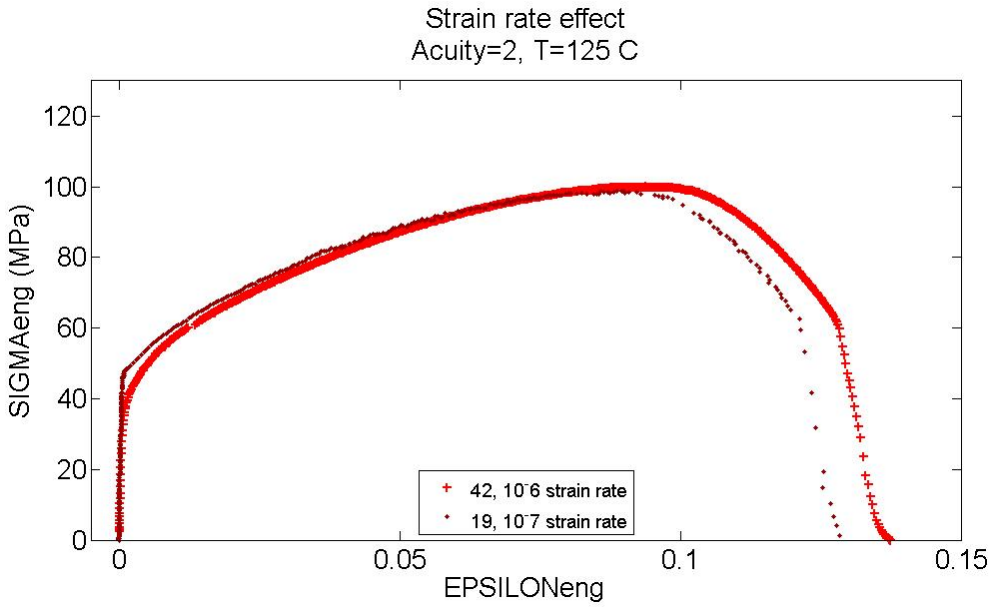

Figure 5.23: Effect of the strain rate on $\sigma - \varepsilon$ curves; the two specimens had notch acuity 2 and were both exposed to 125℃. Lighter red colour indicates the testpiece tested with higher strain rate

Evidently and as expected, a lower strain rate brought to a lower materials resistance and lower failure strain. This effect was more visible on the set of specimen with the blunter notches and higher testing temperature: when the acuity was 2 infact, a difference of 13.9 MPa in the maximum stress was recorded while just a difference of 5.5 MPa was found in the acuity 5 testpieces when the strain rate

was changed. Same observation can be made for the strain to rupture, which was decreased more effectively when blunter notches were introduced.
The effect can reasonably be found in the higher temperature the acuity 2 specimens were exposed to, which brought to a general decrease in the strength properties. This is better explained in the next section.

5.1.2 Effect of the temperature

As reasonably expected the effect of the temperature on the specimens is to decrease their resistance: strain rate and notch geometry being equal, the specimens tested at higher temperature showed lower maximum stresses and failure strains as shown in Figure 5.24, 5.25, 5.26 and 5.27.

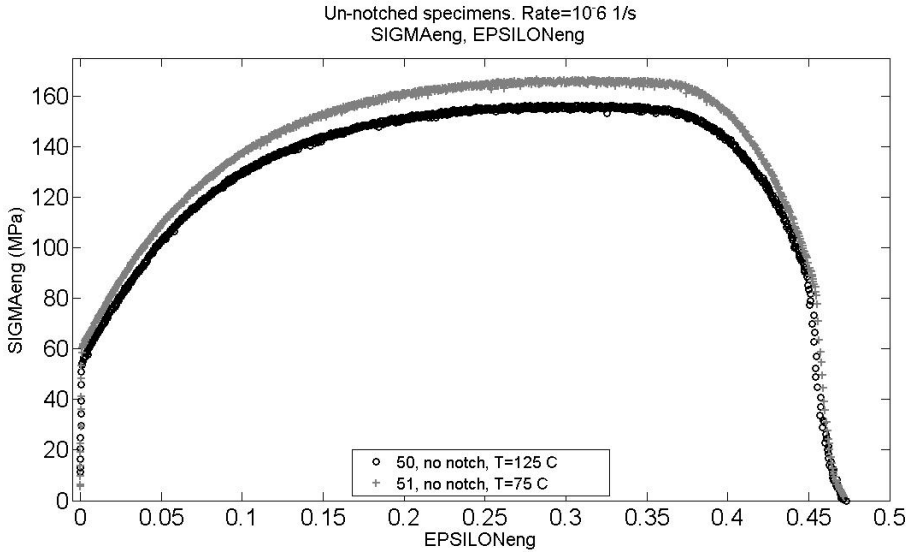

Figure 5.24: Temperature effect on $\sigma - \varepsilon$ curves; the two specimens had no notch and were exposed to 75°C and 125°C

The strain to rupture values for the two smooth specimens made an exception: if the maximum stress was found to be smaller when the temperature was higher, the strain to rupture remained the same.

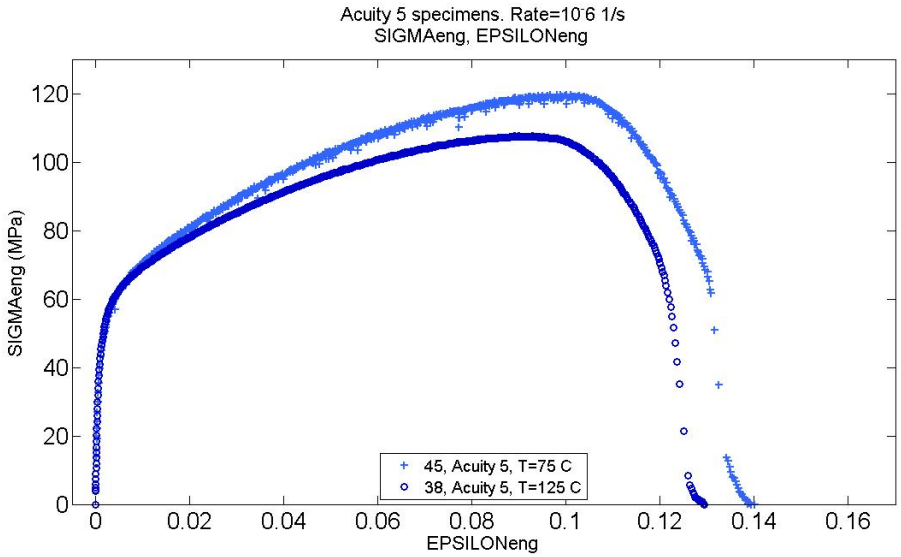

Figure 5.25: Temperature effect on $\sigma - \varepsilon$ curves; the two specimens had notch acuity 5 and were exposed to 75℃ and 125℃

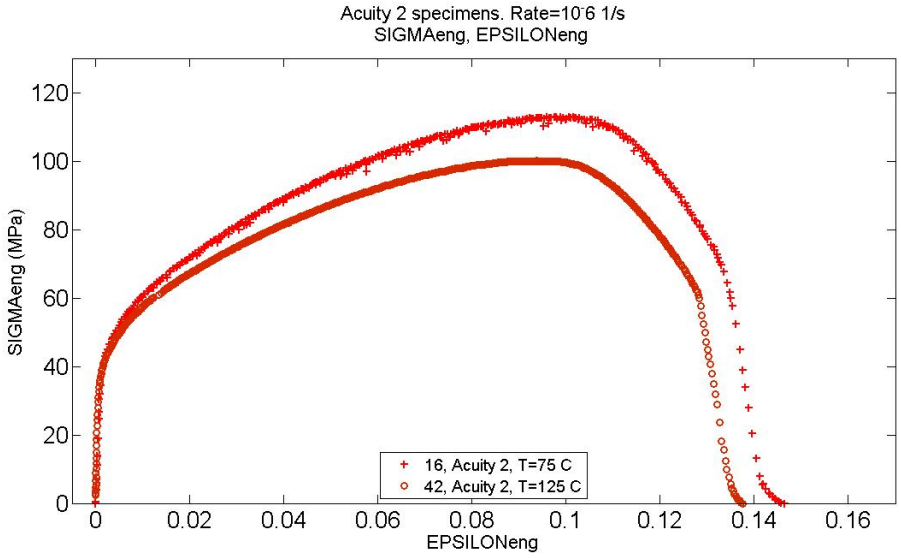

Figure 5.26: Temperature effect on $\sigma - \varepsilon$ curves; the two specimens had notch acuity 2 and were exposed to 75℃ and 125℃

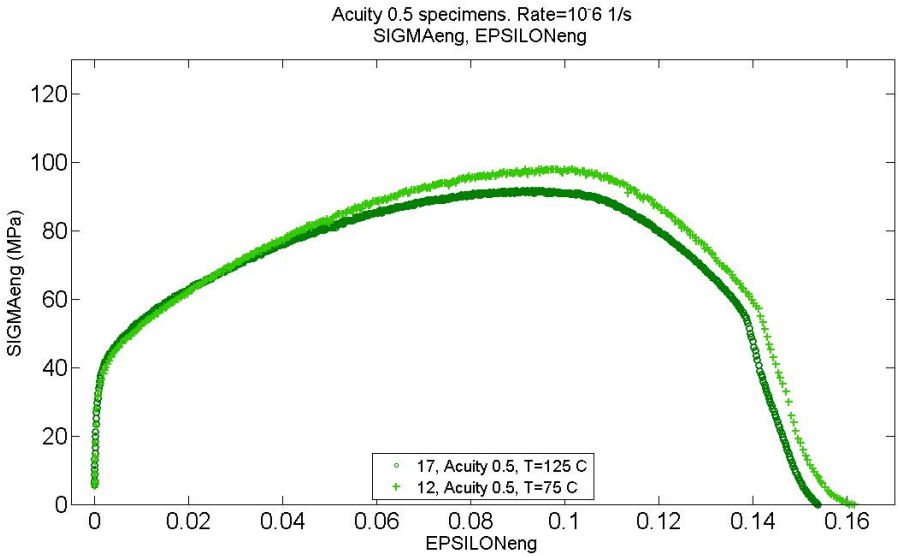

Figure 5.27: Temperature effect on $\sigma - \varepsilon$ curves; the two specimens had notch acuity 0.5 and were exposed to 75°C and 125°C

It is clearly visible how just the plastic region was affected by the raise of temperature, while the elastic trait showed no appreciable modification.
Actually it has to be remarked that the overall effect of the temperature was not appreciable nor significant at all, for the difference in both the maximum stresses and strains to be negligible.

In this case any consideration can be done for the specimen tested at $10^{-7}1/s$ strain rate since the notches had different acuities. It is however reasonable to expect a similar effect even at lower strain rate values.

5.1.3 Effect of the notch acuity

It is interesting to observe how a different induced multiaxial stress state influenced the specimen's resistance values. The notch acuity effect is well evident in Figure 5.28 and 5.29 where the stress-strain curves are divided by exposition temperature.

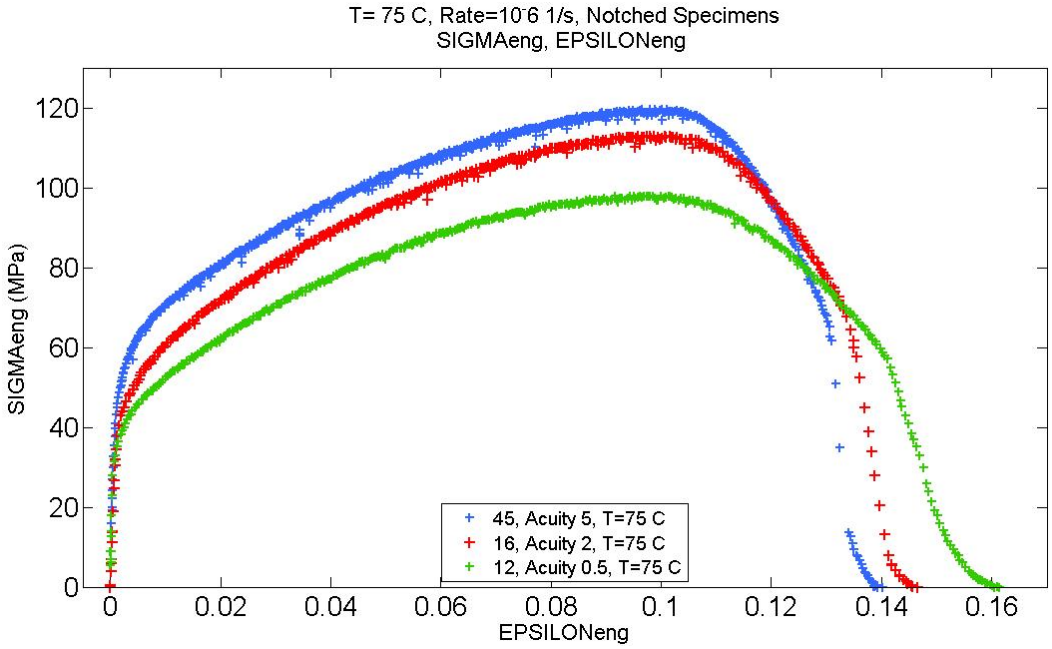

Figure 5.28: Notch acuity effect on $\sigma - \varepsilon$ curves; the three specimens with notch acuity 5, 2 and 0.5 and were exposed to 75°C

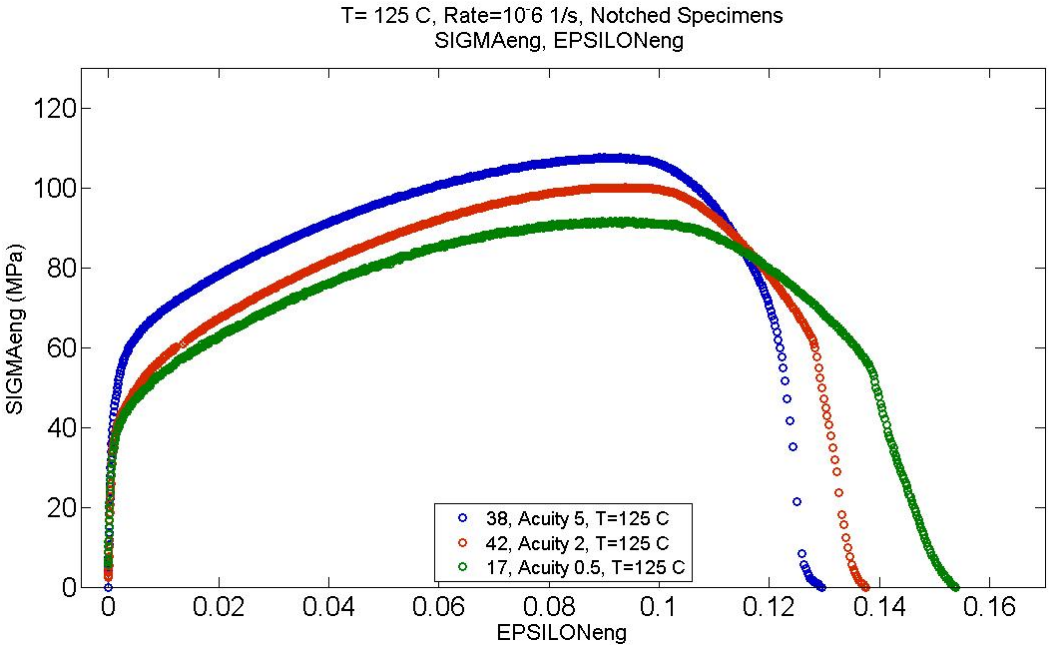

Figure 5.29: Notch acuity effect on $\sigma - \varepsilon$ curves; the three specimens with notch acuity 5, 2 and 0.5 and were exposed to 75°C

The trend that is evident from both the diagram is that, test temperature and strain rate being equal, the higher the ratio A_0/R the higher the UTS and the lower the ultimate tensile strain are.
Moreover, also the yield strength was affected by the notch acuity, resulting in smaller values for the specimens with blunter notches.

What is interesting is that while the maximum strength decreased with an increasing notch acuity, the strain to rupture increased: from 0.139 for specimen's acuity 5, through 0.147 for acuity 2, up to 0.161 for the bluntest notch, the increase was evident but still not significative. Further investigations in this direction have infact to be made.

5.2 Yield Strenght and Notch Strengthening Behaviour

From the engineering curves showed in the first section the values for both the yield stress σ_Y and the maximum stress σ_{max} were extrapolated and they are shown in Figure 5.30. In particular, for copper being a ductile material, the yield strength was not a well defined point and it was considered reasonable to determine it with the 0.2% offset method.
The maximun stress instead was calculated as the higher value reached by the stress in the engineering curve.

ACUITY	STRAIN RATE (s^{-1})	T (°C)	SPEC.NR	σ_Y (MPa)	σ_{max} (MPa)
0	10^{-6}	75	51	62.98	166.55
		125	50	57.2	156.35
5	10^{-6}	75	45	56.99	119.58
		125	38	56.19	107.60
	10^{-7}	75	52	50.39	114.1
2	10^{-6}	75	16	48.39	112.78
		125	42	44.59	100.18
	10^{-7}	125	19	50.58	98.84
0.5	10^{-6}	75	12	40.99	97.98
		125	17	43.19	91.58

Figure 5.30: Summary of the calculated values for the yield strength and the maximum stress for each tested specimen. The values were extracted from the engineering curves

What has been observed is that, other conditions being equal, both the yield strenght and the maximum stress increased with an increasing notch acuity. This is better represented in Figure 5.31 and 5.32 where the specimens tested with $10^{-7}1/s$ strain rate are not reported because no relation was found between the values.

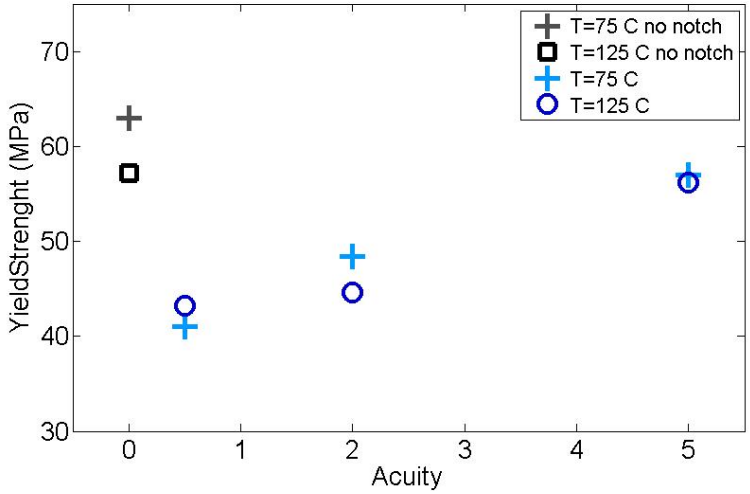

Figure 5.31: Calculated yield strenght in function of notch's sharpness for the specimens tested with $10^{-6}1/s$; the squared points represent the un-notched yield values.

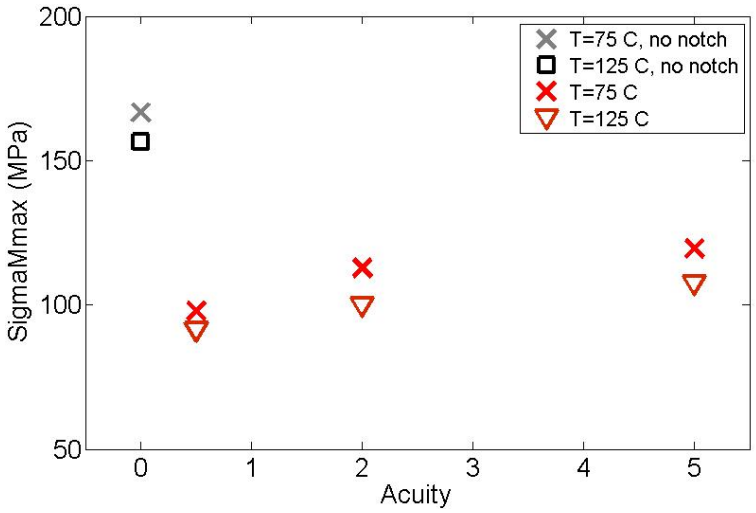

Figure 5.32: Maximum stress in function of notch's sharpness; the squared points represent the un-notched yield values.

An increase in notch acuity from 0.5 to 5 lead to an increase of the yield strength of 30.87 MPa at 75℃ and of 24.5 at 125℃.
The maximum stress instead increased by 40.82 MPa when the notch acuity was increased from 0.5 to 5 at 75℃; at 125℃ the registered increase was 29.19 MPa, suggesting that the acuity had a slightly bigger effect at lower temperatures, although the temperature effect can not be considered as significant as explained in section 1.1.2

Notch sensitivity The parameter that was used in this work to evaluate the notch strengthening or weakening behaviour was the ratio defined as follows:

$$NotchStrength = \frac{\sigma_{max}}{A_{net}} \tag{5.13}$$

where σ_{max} is extracted from the engineering curve and A_{net} is the net cross sectional area calculatd at the base of the notch. It has been calculated also for the smooth specimens so that a comparison could have been made. Infact, as showed in the table in Figure 5.34, because of the plastic constraint at the notch, the ratio is higher for the notch specimens with respect to the un-notched ones. Also, the higher the ratio, the higher the strengthening due to the induced multiaxial stress state is.

ACUITY	STRAIN RATE (s^{-1})	T (°C)	SPEC.NR	σ_{max} / A_{net} (N)
0	10^{-6}	75	51	3.33
		125	50	3.13
5	10^{-6}	75	45	4.79
		125	38	4.31
	10^{-7}	75	52	4.57
2	10^{-6}	75	16	4.51
		125	42	4.01
	10^{-7}	125	19	3.96
0.5	10^{-6}	75	12	3.98
		125	17	3.72

Figure 5.33: Notch strenght values calculated with Equation

From the table in 5.34 it can be seen how the ratio σ_{max}/A_{net} for the notched specimens had an increase from 16 to 30% at both the testing temperature compared to the smooth specimens. Also it can be observe that the notch strength parameter is higher for the testpiece exposed at 75°C, suggesting the notch strength to be temperature sensitive. Moreover the ratio increased with an increasing notch acuity, clearly indicating the material is notch strengthening.

5.3 Time to rupture and ductility evaluation

In Figure 5.34 the time to rupture for each specimen are reported. What is evident and obvious is the large difference between the values obtained with $10^{-6}1/s$ and $10^{-7}1/s$ strain rate. For the latter infact it took 413.28 hours at 75°C when the

notch acuity was 5 and 390.17 hours at 125℃ for the specimen with notch acuity 2. For the specimens tested with $10^{-6}1/s$ strain rate , the time to rupture turned out to be increasing with the notch acuity and this same trend was found for both the testing temperature.

ACUITY	STRAIN RATE (s^{-1})	T (°C)	SPEC.NR	t_r (h)	ε_R
0	10^{-6}	75	51	142.89	0.472
		125	50	143.67	0.473
5	10^{-6}	75	45	42.72	0.139
		125	38	40.28	0.129
	10^{-7}	75	52	413.28	0.134
2	10^{-6}	75	16	44.89	0.147
		125	42	41.33	0.138
	10^{-7}	125	19	390.17	0.123
0.5	10^{-6}	75	12	47.67	0.161
		125	17	45.83	0.154

Figure 5.34: Time to rupture values and engineering strain to rupture values calculated for all the tested specimens

However, the introduction of the notches, of any sharpness, turned out to decrease the materials lifetime. This is more visible if the data from the notched specimens are compared to the smooth ones: at 75℃ infact, the decrease after the introduction of notches with acuity 5, 2 and 0.5 was 100, 98 and 95 hours respectively. At 125℃ instead was about 103, 102 and 98 hours.

Currently, ductility is considered a qualitative, subjective property of a material. For the purpose of the present project it indicates the extent to which the material can be deformed without fracture i.e its ability to flow plastically before fracture [22]. For that reason the engineering strain to rupture was taken as measure of ductility and the calculated values are reported in Figure **??**

Decreasing values of strain to rupture with increasing notch acuity were found: at 75℃ infact the ε_R changed from 0.161 for the specimen with acuity 0.5 to 0.139 when the acuity was 5 and the same trend was found at 125℃.

Anyway, it can be observed that the maximum difference between the strain to rupture values was $\Delta_{R,75} = 2.2\%$ at 75℃ and $\Delta_{R,125} = 2.5\%$ at 125℃, which are too small values to conclude that a ductility change occurred in the specimens. Nevertheless, an increasing trend of the strain to rupture with notch acuity was observed,

as was already visible in the stress-strain curves in Figure 5.28 and 5.29.

It has to be remarked that the the reported values represented the overall axial strain measured within the gauge length of 51 mm and they are not representative of the local deformation within the notches: the local strain in the notches is of course much larger than average overall strain as it is further shown in Section 1.4.

It can be observed that the maximum difference between the ε_R values is $\Delta_{R,75} = 0.019$ at 75℃ and $\Delta_{R,125} = 0.021$ at 125℃, which are too small values to conclude that a ductility change occurred in the specimens. Nevertheless, an increasing trend of the strain to rupture with notch acuity was observed, as was already visible in the stress-strain curves in Figure 5.28 and 5.29.

5.4 Shape Changes Within the Notches

In the present section the observed shape changes in the notched bar specimens during the tests are described.
Notch dimentions has been measured for each specimen before and after the tensile tests: values for both the broken and the unbroken notch can be found in Figure 5.35

. The two parameters which were used to characterise the notches deformation are the axial strain reduction for the unbroken notches (equation 5.14)and the radial strain reduction in both the broken and unbroken ones (equation 5.15)

$$\varepsilon_A\% = \frac{L_f - L_0}{L_f} \cdot 100 \tag{5.14}$$

$$\varepsilon_R\% = \frac{A_0 - A_f}{A_0} \cdot 100 \tag{5.15}$$

where L_0 is the intial notch length which was equal to 1.12 mm for the acuity 5 notches, 2.82 for the acuity 2 and 6.65 for the acuity 0.5; L_f is the final measured length of the unbroken notche. In equation 5.15 instead, A_0 is the area of the original cross section, calculated with the measured values of the specimen's diameter and A_f is the minimum cross sectional area after fracture.
SEM images of the fractured sections were used to calculate the final area; from Figure5.38 to 5.42 the fractured areas and how they have been calculated are shown. The images of just four specimens (one for each set of acuity) are reported for practical reasons: the fractured area was identified and highlighted in black, then

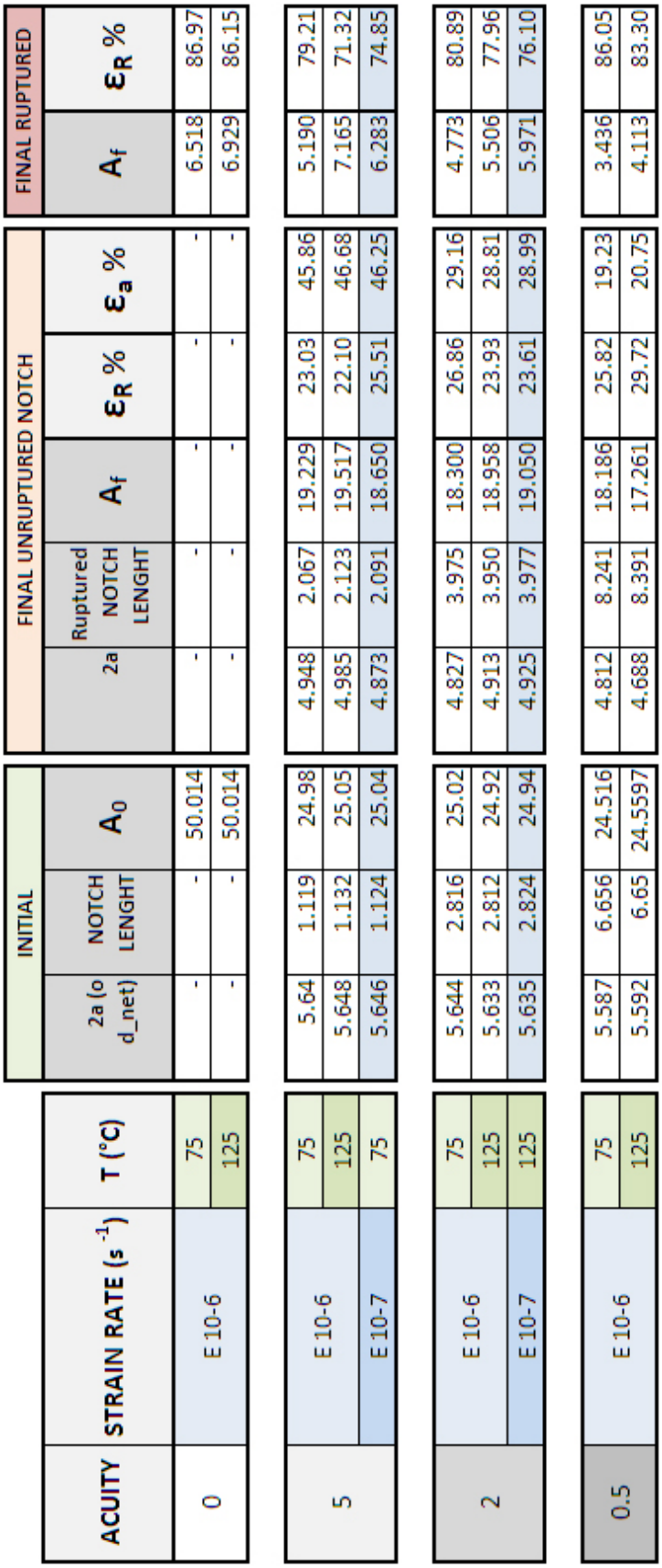

ACUITY	STRAIN RATE (s^{-1})	T (°C)	INITIAL			FINAL UNRUPTURED NOTCH					FINAL RUPTURED	
			2a (o d_net)	NOTCH LENGHT	A_0	2a	Ruptured NOTCH LENGHT	A_f	ε_R %	ε_a %	A_f	ε_R %
0	E 10-6	75	-	-	50.014	-	-	-	-	-	6.518	86.97
		125	-	-	50.014	-	-	-	-	-	6.929	86.15
5	E 10-6	75	5.64	1.119	24.98	4.948	2.067	19.229	23.03	45.86	5.190	79.21
		125	5.648	1.132	25.05	4.985	2.123	19.517	22.10	46.68	7.165	71.32
	E 10-7	75	5.646	1.124	25.04	4.873	2.091	18.650	25.51	46.25	6.283	74.85
2	E 10-6	75	5.644	2.816	25.02	4.827	3.975	18.300	26.86	29.16	4.773	80.89
		125	5.633	2.812	24.92	4.913	3.950	18.958	23.93	28.81	5.506	77.96
	E 10-7	125	5.635	2.824	24.94	4.925	3.977	19.050	23.61	28.99	5.971	76.10
0.5	E 10-6	75	5.587	6.656	24.516	4.812	8.241	18.186	25.82	19.23	3.436	86.05
		125	5.592	6.65	24.5597	4.688	8.391	17.261	29.72	20.75	4.113	83.30

Figure 5.35: Dimentions and deformation of notches before and after rupture. Data are reported for both the broken and unbroken notches

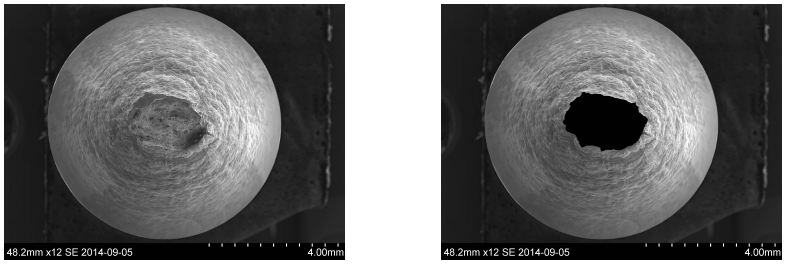

Figure 5.36: Specimen nr.12 with acuity 0.5, tested at $10^{-6}1/s$ strain rate and 75℃. Broken section 1: SEM image on the left and the calculated area in black on the right

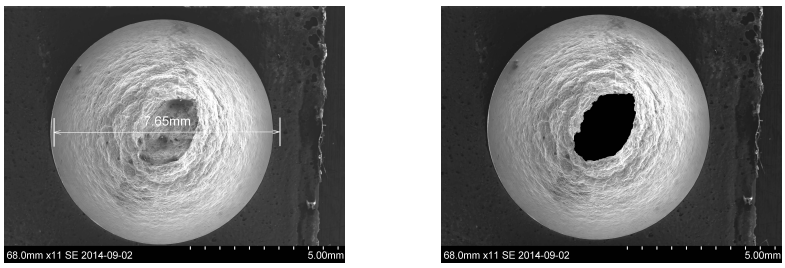

Figure 5.37: Specimen nr.12 with acuity 0.5, tested at $10^{-6}1/s$ strain rate and 75℃. Broken section 2: SEM image on the left and the calculated area in black on the right

the area was calculated with Photoshop software.

The so calculated for the axial and radial strain were found to have no relation for the unbroken notches, while an in the broken ones the radial strain showed an increasing trend with a decreasing notch acuity. The maximum percentage reduction of area was infact found in the smooth specimens, namely 86% reduction at both $125 and 75$℃; the two specimens with acuity 5, accordingly to the trend, experienced the smaller area reduction, with values around 71% and 79%. No such consideration can be made for the specimens tested at $10^{-7}1/s$ due to lack of data.

It can be observed how the local radial strain reduction with the notch acuity

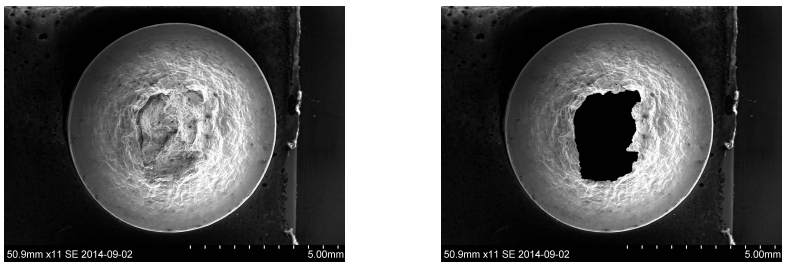

Figure 5.38: Specimen nr.42 with acuity 2, tested at $10^{-6}1/s$ strain rate and 125℃. Broken section 1: SEM image on the left and the calculated area in black on the right

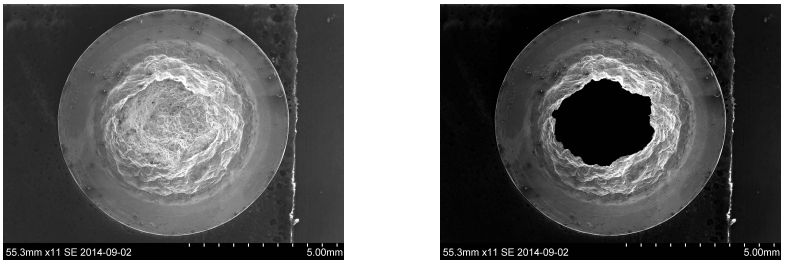

Figure 5.39: Specimen nr.38 with acuity 5, tested at $10^{-6}1/s$ strain rate and 125℃. Broken section 1: SEM image on the left and the calculated area in black on the right

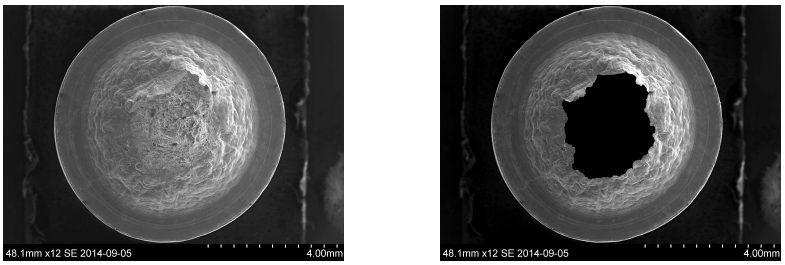

Figure 5.40: Specimen nr.38 with acuity 5, tested at $10^{-6}1/s$ strain rate and 125℃. Broken section 2: SEM image on the left and the calculated area in black on the right

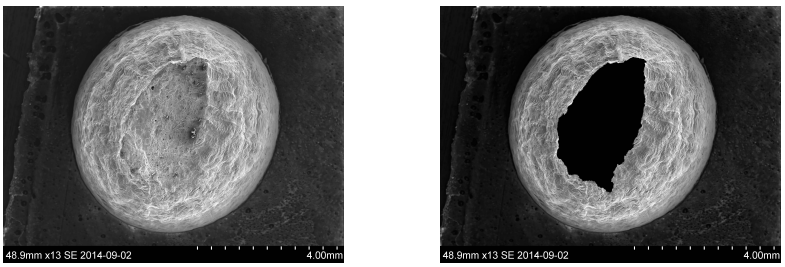

Figure 5.41: Un-notched specimen nr.51, tested at $10^{-6}1/s$ strain rate and 75℃. Broken section 1: SEM image on the left and the calculated area in black on the right

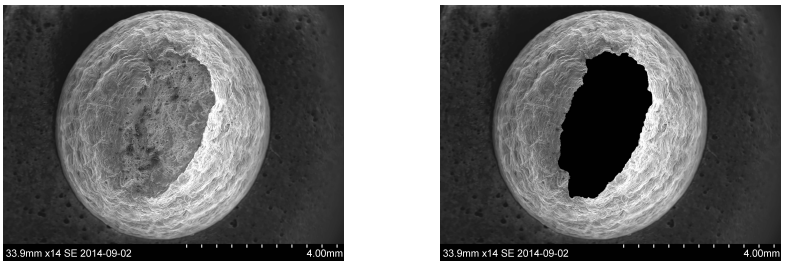

Figure 5.42: Un-notched specimen nr.51, tested at $10^{-6}1/s$ strain rate and 75℃. Broken section 1: SEM image on the left and the calculated area in black on the right

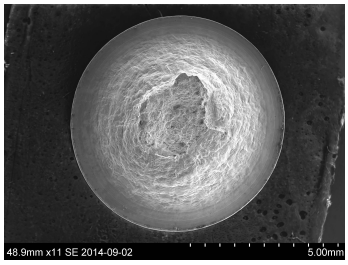

(a) Broken section 1

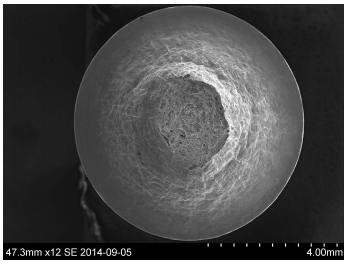

(b) Broken section 2

Figure 5.43: SEM images of specimen nr.16, notch acuity 2 tested at $10^{-6}1/s$ strain rate and 75°C

follows the same trend as both the time to rupture and the strain to rupture: the three parameters increase with the notch sharpness at both the testing temperature. This leads to the conclusion that in the material an higher concentration of stresses induces a small but still appreciable ductility reduction hence a decrease in the component's lifetime.

5.5 Metallographic investigations

As described in Chapter 4 one specimens was chosen for post test metallography, namely the specimen 16 with notch acuity 2, tested with $10^{-6}1/s$ strain rate at 75°C. Both the broken notch and the unbroken one were examined by cutting the specimen in its longitudinal middle section so that investigation on the mode of fracture could have been made. Also, an untested specimen, was sectioned and analyzed at LOM so that it could provide the original microstructure for comparison.
In Figure 5.43 SEM pictures of the failed specimens broken sections are showed: it is evident how a ductile fracture occurred, for the failure surface having a dimpled aspect and a cup-and-cone shape.

In figure 5.44 and 5.45 the microstructure of the broken notch is showed: it is evident how the grain size is smaller in correspondence of the fracture while an averagely mixed grain size is found far away from the edges. Also, an higher number of elongated grains along the loading direction were found closer to the failure region

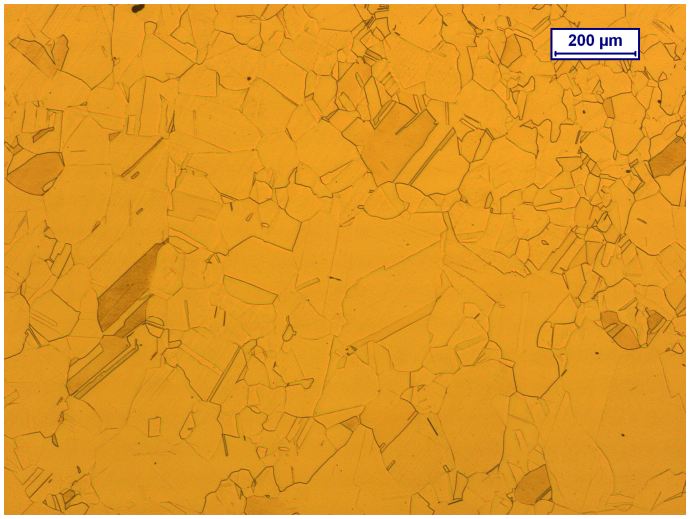

Figure 5.44: Specimen nr.16 tested at 75℃ with $10^{-7}1/s$ strain rate. Image taken at 10x magnification in a area far from the notch. Image taken with 5x magnification in a region far from the broken notch.

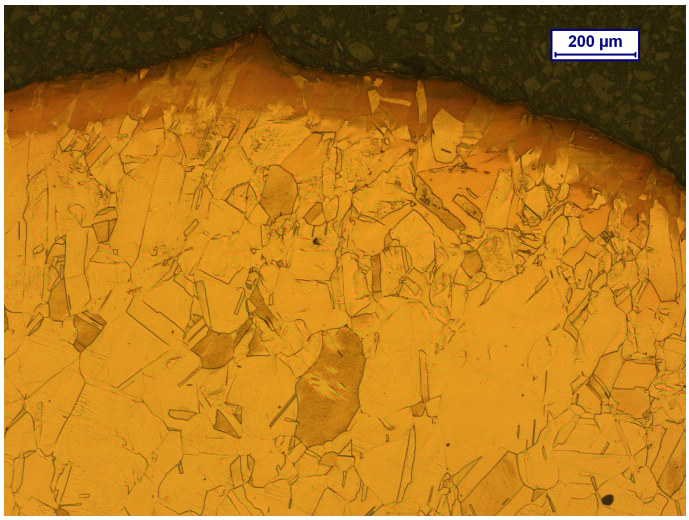

Figure 5.45: Specimen nr.16 tested at 75℃ with $10^{-7}1/s$ strain rate. Image taken at 10x magnification in a area far from the notch. Image taken with 5x magnification at the center of the broken notch

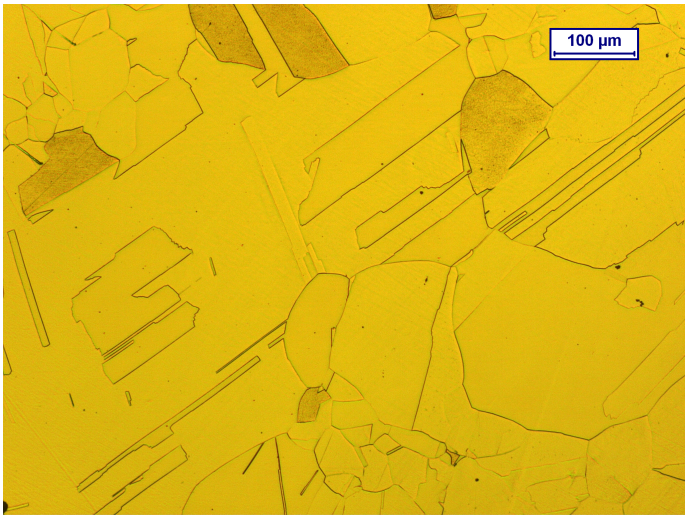

Figure 5.46: Specimen nr.16 tested at 75°C with $10^{-7}1/s$ strain rate. Image taken at 10x magnification in a area far from the notch. Some elongated grains with 45° orientation are visible

At 10x it was possible to better appreciate the grains alignment throuout the sample: far from the fracture infact, many 45 degrees aligned and elongated grains were found as shown in Figure 5.46.

For the unbroken notch just pictures at 5x were taken. Here again it can be observed an homogeneous grains dimention and orientation far from the notch (5.47)and aligned elongated ones in the notch throat, suggesting the region to be subjected to higher stresses, hence stronger plastic deformation (5.49). Also, finer grains were found on the surface around the minimum cross section.

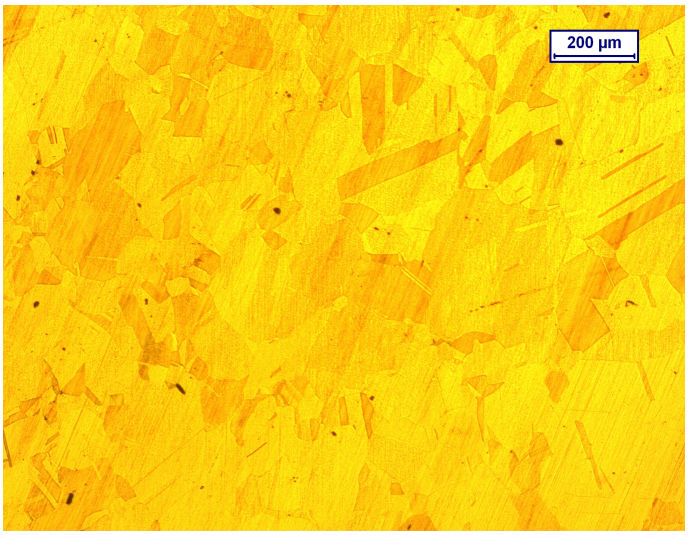

Figure 5.47: Specimen nr.16 tested at 75°C with $10^{-7}1/s$ strain rate. Image taken with 5x magnification in a region far from the unbroken notch

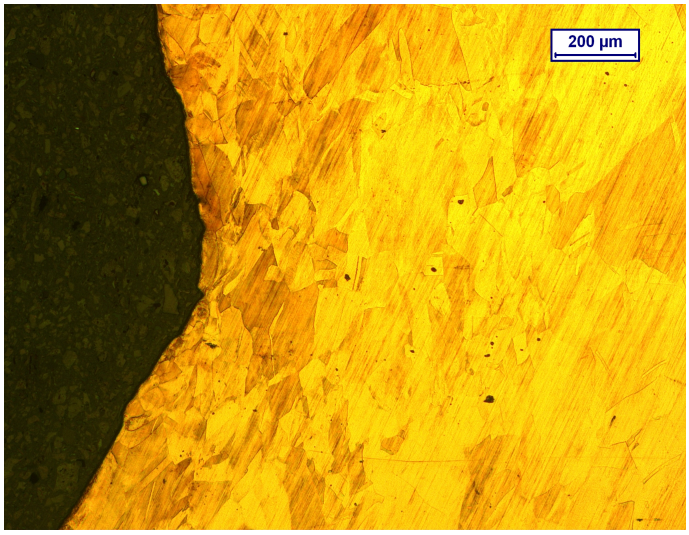

Figure 5.48: Specimen nr.16 tested at 75°C with $10^{-7}1/s$ strain rate. Image taken with 5x magnification at the center of the unbroken notch: aligned grains in corispondence of the notch throat and finer grains on the notch's surface.

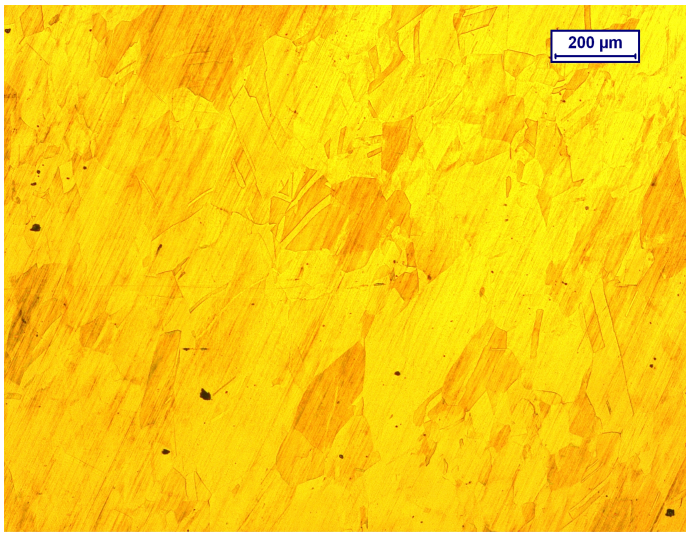

Figure 5.49: Specimen nr.16 tested at 75°C with $10^{-7}1/s$ strain rate. Image taken at 10x magnification in a area far from the notch. Image taken with 5x magnification at the center of the unbroken notch.

In Figure 5.50 the specimen's original mixed microstructure is shown: here it can be appreciate the difference in the grain size and shape before and after testing

Figure 5.50: Specimen 43, not tested. The specimen's original microstructure shows mixed grains size and orientation.

Unfortunately, the magnification in the optical microscope was not enough to allow cavities observation but it is reasonable to expect the failure occurred by void nucleation and coalescence.

Conclusions

The influence of multiaxial stress state on Cu-OFP mechanical properties has been studied by means of slow strain rate tensile tests on double notched specimens: two were the strain rate used, $10^{-6}1/s$, $10^{-7}1/s$ and two were the testing temperature 75℃ and 125℃. Three were the set of specimen's notch acuity, namely 5, 2 and 0.5. The following conclusions can be drawn:

- Both the yield strength and maximum strength were found to be higher for specimens with higher acuity: a more localised stress field increases material's strength properties.
- The strain rate has more influence on the bluntest notches than in the sharper ones but the effect is not to be considered to be significantly influencing the material's strength properties.
- The effect of the temperature was not appreciable nor significant at all, for the difference in both the maximum stress and strain to be negligible.
- The introduction of U-shaped double notches on the material has the effect to decrease the component's lifetime to an extent that is proportional to the notch's sharpness.
- The material's ductility turned out to be affected by the notch acuity for a small extent: the sharper the notch, the smaller the strain to rupture
- The shape changes within the notches were found to be higher on the ruptured one but was not found to be any trend in the axial and radial strain reduction values. More tests are needed to be performed with different strain rates and notch acuity.

Bibliography

[1] *"A sustainable energy and climate policy for the environment, competitiveness and long-term stability, Swedish government Nuclear Energy Policy document officially ending Sweden's nuclear phase-out policy", February 5, 2009, p. 3, www.sweden.gov.se..*

[2] D.G. Bennet, R.Gens, *"Overview of European concepts for high level waste and spent fuel disposal with special reference waste container corrosion"*, Journal of Nuclear Materials.

[3] B.Rosborg, L.Werme, *"The Swedish nuclear waste program and the long term corrosion behaviour of copper"*, Journal of Nuclear Materials.

[4] *http://www.test.org/doe/.*

[5] *http://www.world-nuclear.org/info/Country-Profiles/Countries-O-S/Sweden/.*

[6] *https://sweden.se/society/energy-use-in-sweden.*

[7] B. Stiller, T. Bocek, F. Hecht, G. Machado, P. Racz, M. Waldburger, *"Long-term safety for the final repository for spent nuclear fuel at Forsmark"*, Svensk Kärnbränslehantering AB, 2011.

[8] B. Stiller, T. Bocek, F. Hecht, G. Machado, P. Racz, M. Waldburger, *"RandD Programme 2010: programme for research, development and demonstration of methods for the management and disposal of nuclear waste"*, Svensk Kärnbränslehantering AB, 2010.

[9] *"Fuel and canister process report for the safety assessment SR-Site"*, Svensk Kärnbränslehantering AB, 2010.

[10] Xuexing Yao, Rolf Sandström, *"Study of creep behaviour in P-doped copper with slow strain rate tensile tests"*, Department of Materials Science and Engineering, Royal Institute of Technology (KTH), 2000.

[11] Rolf Sandström, *"Basic Model for primary and secondary creep in copper"*, Acta Materialia, 2011.

[12] Rolf Sandström, Sakander Waqas Ahmad, Kirti Teja Pasupuleti, Meysam Mahdavi Shahri, *"Basic Model for primary and secondary creep in copper"*, Department of Materials Science and Engineering, Royal Institute of Technology (KTH), 2000.

[13] Joseph R. Davis, *"Copper and Copper Alloys"*, ASM International, 2001.

[14] Heikki Raiko, Rolf Sandström, Håkan Rydén, Magnus Johansson, *"Design analysis report for the canister"*, VTT, Materials Science and Engineering KTH, Svensk Kärnbränslehantering AB, 2010.

[15] Kirti Teja Pasupuleti *"Slow strain rate testing of welded copper"*, Material Science and Engineering, KTH, 2012.

[16] Rolf Sandström, Sakander Waqas Ahmad, Kirti Teja Pasupuleti, Meyasam Mahdavi Shahri, *"Slow strain rate tensile testing of friction stir welded Cu-OFP; constitutive equations for creep"*, Department of Materials Science and Engineering, KTH.

[17] Rui Wu, Facredin Seitisleam, Rolf Sandström, *"Creep Properties of phosphorus alloyed oxygen free copper under multiaxial stress state"*,Swerea KIMAB, Department of Materials Science and Engineering, KTH, 2009.

[18] Rolf Sandström, Josefin Hallgren, *"The role of creep in stress strain curves for copper"*, Journal of Nuclear Materials, 2011.

[19] G.A Webster, S.R Holdsworth, M.S Loveday, K.Nikbin, I.J. Perrin, H. Purper, R.P. Skelton, M.W. Spindler, *"A code of Practice for conducting notched bar creep tests and for interpreting the data"*, Loveday M S, Gibbons T B, Blackwell Publishing Ltd, 2004

[20] Johan Pilhagen, *"Manual for the electromechanical tensile/compression testing system NT2005 (Model 41-E)"*, Material Science and Engineering Department, KTH, 2014.

[21] Xuexing Yao, Rolf Sandström, *"Study of creep behaviour in P-doped copper with slow strain rate tensile tests"*, Material Science and Engineering Department, KTH, 2000.

[22] Joseph R. Davis, *"Tensile Testing"*, ASM International, 2004.

Acknowledgements

I wish to express my sincere thanks to prof. Irene Calliari and Rolf Sandström for having given me this important opportunity: to carry out my thesis project at the KTH in Stockholm was a great chance for me to learn and grow. I would also thank Fangfei, my tutor and friend, and the Material's Technology group for all the support they gave me.

A big thanks to my friends and classmates from University for all the good time and sincere friendship.

A special thanks to my mum and my family, with whom I would have never come so far.